Seismic evidence for velocity heterogeneity along ~40 Ma old oceanic crustal segment formed at the slow-spreading Mid-Atlantic Ridge in the equatorial Atlantic Ocean from full waveform inversion of ocean bottom seismic data

Peng Guo[1] and Satish C. Singh[2]

[1]Deep Earth Imaging Future Science Platform, The Commonwealth Scientific and Industrial Research Organisation (CSIRO), Kensington, Western Australia, Australia

[2]Institut de Physique du Globe de Paris, Université Paris Cité, CNRS, Paris, France

Corresponding author: Peng Guo (peng.guo@csiro.au)

Key Points:

- We apply full waveform inversion to the crustal turning waves recorded by ocean bottom seismometers in the equatorial Atlantic Ocean.
- The velocity model exhibits strong crustal velocity heterogeneity, containing four distinct segments correlating well with seafloor morphology.
- The strong crustal heterogeneity seems to be caused by a combination of magmatic and tectonic processes, along with chemical heterogeneity in the mantle.

Abstract

In slow spreading environments, oceanic crust is formed by a combination of magmatic and tectonic processes. Tomographic studies suggest that a magmatically accreted crust consists of an upper crust containing basaltic lava flows and dike and a lower crust comprising of gabbro, whereas the tectonically controlled crust may have gabbros and serpentinite close to the seafloor. Using full waveform inversion applied to ocean bottom seismometer data, we reveal the presence of a strong lateral variability in the 40 – 48 Ma old oceanic crust in the slow-spreading equatorial Atlantic. Over a 120 km-long section between the St Paul fracture zone (FZ) and the Romanche transform fault (TF), we observe four distinct 20-30 km long crustal segments. The segment affected by the St Paul FZ consists of three layers, 2 km thick layer with velocity <6 km/s, 1.5 km thick middle crust with velocity 6-6.5 km/s, and an underlying layer with velocity ~7 km/s in the lower crust. The segment associated with an abyssal hill morphology contains high velocity ~7 km/s from a shallow depth of 2 – 2.5 km below the basement, indicating the presence of either serpentinized peridotite or primitive gabbro close to the seafloor. The segment associated with a low basement morphology seems to have 5.5 – 6 km/s velocity starting near the basement extending down to a depth of 4 km, indicating chemically distinct crust. The segment close to the Romanche transform fault, a normal oceanic crust with velocity 4.5-5 km/s near the seafloor indicates a magmatic origin. The four distinct crustal segments have a good correlation with the overlying seafloor morphology features. These observed strong crustal heterogeneities could result from alternate tectonic and magmatic processes along the ridge axis, possibly modulated by chemical variations in the mantle.

Plain Language Summary

The classic magmatically accreted oceanic crust usually has a nearly uniform structure. The speed of seismic waves, which is widely used as a proxy for the physical properties of the Earth, is relatively low in the upper crust however increases rapidly with depth, while in the lower crust the velocity is high but increases more slowly. Nevertheless, oceanic crust formed at the slow-spreading mid-ocean ridges can be very heterogeneous. However, it is challenging to quantify the nature of this heterogeneity using conventional travel time based analysis.

Here we apply the cutting-edge full waveform inversion technique to an ocean bottom seismometer dataset from the equatorial Atlantic Ocean. The aim is to create seismic velocity models of oceanic crust with enhanced details. We reveal four distinct zones within a 120-km long section, with boundaries consistent well with the seafloor morphology. The section contains two segments of classic oceanic crust, a segment with high velocities at shallow depth, possibly containing serpentinized mantle peridotite and olivine-rich gabbro indicating tectonic origin, and a chemically distinct segment with few velocity variations along depths. The observed strong crustal heterogeneities seem to result from a combination of magmatic and tectonic accretion process induced by chemically heterogeneous mantle.

1 Introduction

Oceanic crust is formed at the Mid-Ocean Ridges (MORs) from basaltic melt derived from the decompression of upwelling mantle beneath the ridges. Insights gained from studies of ophiolites (e.g., Salisbury & Christensen, 1978; Nicolas et al., 1988; Boudier et al., 1996; Kelemen et al., 1997; Kelemen et al., 2020), ocean drilling results (e.g., Alt et al., 1996; Miller & Christensen 1997; Iturrino et al., 2002; Carlson & Miller, 2004; Wilson et al., 2006; Swift et al., 2008) and geophysical studies (e.g., Spudich & Orcutt, 1980; White et al., 1992; Harding et al., 1993; Toomey et al., 1994; Canales et al., 2005; Singh et al., 2006; Carbotte et al., 2013; Grevemeyer et al., 2018; Christeson et al., 2019; Vaddineni et al., 2021) suggest that, the crust formed by the magmatic process can be divided into two distinct layers, an upper (layer 2) and a lower crust (layer 3), with the sediments above the basement being layer 1. The upper crust is primarily composed of pillow lavas and the underlying sheeted dikes, and is characterized by a high

seismic velocity gradient (1 - 2 s^{-1}) where the velocity increases from ~3.5 to ~ 4.5 km/s at top of the layer to 6 - 6.5 km/s at the bottom. The lower oceanic crust contains mainly gabbroic rocks where the velocity increases more slowly with depth (~ 0.1 s^{-1}) from ~6.5 km/s to ~ 7 km/s (Christeson et al., 2019). The thickness of the lower crust is usually about twice of that of the upper crust.

However, the accretionay mechanism can vary with the spreading rate (Morgan & Chen, 1993; Carbotte et al., 2016). At the fast and intermediate spreading ridges, the magmatic process dominates with a fairly unform crustal thickness and structure (Kent et al., 1994; Toomey et al., 1994; Carbotte et al., 2013; Han et al., 2016). At the slow spreading ridges, the magma supply could vary spatially and temporally (Lin & Morgan 1992; Cannat 1993), leading to a heterogeneous crust (Detrick et al., 1995; Canales et al., 2000; Hooft et al., 2000; Escartín et al., 2008; Dunn et al., 2017; Davy et al., 2020). For example, when the magma supply is low, the tectonic process would dominate (Cannat, 1993), leading to the development of oceanic core complexes (OCCs) (Cannat, 1993; MacLeod et al., 2002; Dick et al., 2008; Grevemeyer et al., 2018b), which are formed through the exhumation of mantle ultramafic and lower crustal gabbroic rocks at shallow depth and on the seafloor along long-lived detachment faults (Cann et al., 1997; Cannat et al., 1997; Dick et al., 2000; Blackman & Collins, 2010; Canales, 2010; Xu et al., 2020).

Many recent seismic surveys have revealed heterogeneous crustal structures in the Atlantic Ocean (Canales 2010; Dunn et al., 2017; Escartín et al., 2017; Gregory et al., 2021), which usually coincide with extensive faulting, long-lived detachment faults or the presence of corrugated massifs associated with OCCs. For example, using travel-time tomography in the 60-75 Million years (Ma) old central Atlantic, Davy et al. (2020) revealed the coexistence of normal

oceanic crust and tectonically dominated crust across five ridge segments separated by a transform fault and three nontransform offsets. A review of oceanic crustal models (Christeson et al., 2019) suggests that the crustal thickness and velocity profiles have the greatest standard deviations for the slow-spreading crust attributed to the heterogeneity in the crustal accretion process. Furthermore, hydrothermal alteration can also change rock properties of oceanic crust (Alt et al., 1996; Christeson et al., 2007; Carlson 2011; Audhkhasi & Singh 2019; Boulahanis et al., 2022). Seismic surveys and oceanic drilling have discovered low velocity anomalies above the roof of axial melt lens (Singh et al., 1999) and at the dike-gabbro transition (Swift et al., 2008), which are interpreted to be due to hydrothermal alteration. During a tectonically-dominated crustal accretion, hydrothermal circulation can lead to hydration of crustal rocks and serpentinization of mantle olivine-rich peridotite (Minshull et al., 1998).

Most of the studies of oceanic crust are based on travel-time tomography of crustal and mantle arrivals (e.g., Minshull et al., 1991; White et al., 1992; Toomey et al., 1994; Korenaga et al., 2000; Canales et al., 2005; Escartín et al., 2017; Grevemeyer et al., 2018b; Gregory et al., 2021; Wang & Singh, 2022). This technique is based on a high-frequency approximation and ray assumption for fitting the observed and computed travel times of seismic arrivals (Van Avendonk et al., 1998), resulting in subsurface velocity models that contain mainly large-scale structures. Moreover, travel-time tomography can fail when velocity anomalies are characterized by the same order wavelength as of the seismic waveforms (Luo and Schuster, 1991). On the other hand, full waveform inversion (FWI) (Tarantola, 1984; Shipp & Singh, 2002; Virieux & Operto, 2009), that is based on a full solution of elastic wave equation and utilizes complete waveform information, has the great potential for inferring crustal models with enhanced

accuracy and higher resolution (e.g., Singh et al., 1999; Canales 2010; Christeson et al., 2012; Qin & Singh 2017; Arnoux et al., 2017; Górszczyk et al., 2017; Davy et al., 2021; Arnulf et al., 2021; Guo et al., 2022). Here, we apply FWI to the crustal turning arrivals of the active-source ocean bottom seismometer (OBS) data for estimating high-resolution model of the oceanic crust in the equatorial Atlantic Ocean.

2 Study Area

Our study area lies in the equatorial Atlantic Ocean where the slow spreading Mid-Atlantic Ridge (MAR) is offset by ~1800 km by a set of closely-spaced, large-offset (> 300 km) transform faults (TFs) (Bonatti et al., 1994), from north to south including the St. Paul, the Romanche, and the Chain TFs, with an age variation of 90 Ma over a distance of 400 km (Figure 1). Large-offset TFs may have profound effects on the thermal structure and the dynamics of the mantle upwelling, the melt budget and the composition (heterogeneity) of the migrated melt (Bonatti et al., 1994). The OBS seismic profile of this study is located between the St. Paul fracture zone (FZ) and the Romanche TF (Figure 1). The St. Paul TF, which contains four strike-slip faults and three short intra-transform ridge segments, offsets the MAR by ~600 km. The sub-areal St Paul Island consists of a transpressional ridge containing peridotite with various degrees of serpentinization and deformation (Maia et al., 2016). The Romanche TF offsets the MAR by the largest offsets on Earth of ~880 km, with a 45 Ma lithospheric age contrast. It exhibits a ~20 km wide transform valley and a thick hanging sediment basin in the north flank. Seafloor dredgings at the Romanche TF (Bonatti 1968; Bonatti & Honnorez 1976; Seyler & Bonatti 1997) show an extensive presence of basalt and gabbro on the north flank, but predominantly mantle-

144 derived serpentinized and mylonitic peridotites on the valley floor and in the south of the fault
145 zone. This observation is consistent with the heterogeneous tomographic velocity model obtained
146 across the Romanche transform valley, which is characterized by a mafic crustal structure of
147 average thickness ~6 km in the north of the TF and a magma-reduced crust with variable
148 thicknesses of 4 - 6 km in the south flank (Gregory et al., 2021).
149
150 Recent travel-time tomographic studies using wide-angle OBS data have revealed a nearly
151 constant crustal thickness of 5.6 – 6 km between the St Paul FZ (Growe et al., 2021) and the
152 Romanche TF (Gregory et al., 2021), resembling a normal oceanic crust. Wang and Singh (2022)
153 found that crustal thickness along the 850-km long profile crossing five segments in this region
154 is uniform, indicating more a 2D sheet-like mantle upwelling as compared to 3D plume-like
155 upwelling suggested for slow spreading ridges (Dunn et al., 2005).
156
157

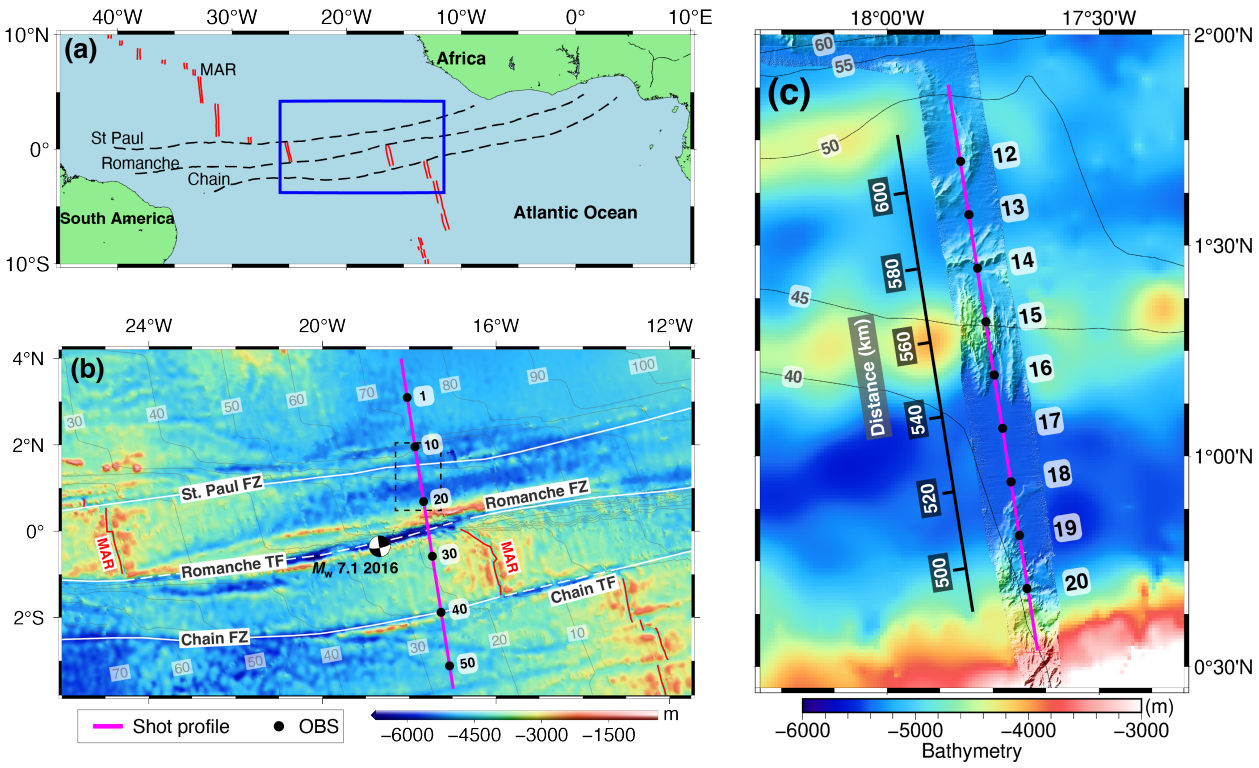

Figure 1. Map of the study area and active-source seismic survey in the equatorial Atlantic Ocean. (a) The equatorial Atlantic Ocean, with the double red lines indicating the Mid-Atlantic Ridge and the dashed black lines showing the St Paul, the Romanche and the Chain TFs and FZs from north to south. The blue rectangle shows the map area in (b). (b) Bathymetry of the ocean bottom seismic survey (zoom-in of the blue rectangle in (a)) with the major oceanic TFs (dashed white lines) and FZs (solid white lines). The black-white beachball indicates the 2016 Mw7.1 Romanche earthquake (Hicks et al., 2020). The black circles suggest the locations of the ocean bottom seismometers (OBSs) with every 10 OBSs plotted for a total of 50 OBSs from the ILAB-SPARC experiment, and the pink line shows the shot profile for the survey (Wang and Singh, 2022). The light grey lines suggest plate ages labelled every 10 Myr (Müller et al., 2008). (c) Close-up of the area (the dashed rectangle in (b)) for the 9 OBSs (12-20) used in this study. The bathymetry was plotted by superimposing the high-resolution bathymetry data collected during

171 the ILAB-SPARC seismic experiment on a relatively low-resolution global bathymetry grid. The
172 pink line passing through the OBSs shows the shot profiles used for inversion. The plate ages
173 were plotted using the light grey lines and labelled every 5 Myr (Müller et al., 2008).

174

175 **3 Data and methods**

176 **3.1 The active-source wide-aperture ocean bottom seismic data and processing**

177 The field data was acquired during the ILAB-SPARC cruise in October-November 2018 onboard
178 the French R/V *Pourquoi Pas?*. A total of 50 OBSs were deployed along a 700-km long section
179 across the St Paul FZ, the Romanche TF and the Chain FZ from north to south, with an average
180 spacing of 14.2 km to record the wide-angle seismic wave refraction and reflection arrivals. The
181 shooting line was extended by 50 km in the south, and 100 km in the north, for a total of 850 km
182 long. All OBSs were equipped with a hydrophone (measuring pressure) and three geophones
183 (measuring vertical and horizontal displacements), with a sampling frequency of 250 Hz. The
184 seismic source used in the survey comprised of two sub-arrays with 8 guns on each array,
185 producing a total volume of 4990 cubic inch, which was fired every ~300 m along the profile.

186

187 We used a part of these data (9 OBSs, the hydrophone component) between the St.Paul FZ and
188 the Romanche TF covering 40 – 48 Ma old oceanic crust for a 120-km long section (Figure 1c).
189 We limited the data processing prior to FWI to a minimum to preserve the original waveform
190 information. A predictive gapped deconvolution was applied to the OBS data to suppress the
191 bubble effects from the air-gun sources while keeping the waveform of the primary arrivals,
192 where we set the first lag of prediction filter as 0.2 s and the lag default was 0.8 s. Then we

applied a zero-phase bandpass filtering of 3 – 10 Hz to the processed OBS data. We also performed 3D to 2D transformation (Pica et al., 1990; Forbriger et al., 2014) to the data, including multiplying the amplitudes of field data by $\sqrt{t}$, where t is the two-way travel-time, and convolving with $1/\sqrt{t}$, because 2D elastic wave equation modeling is used for simulating seismic data recorded in a 3D Earth. Clear crustal turning waves (Pg) with high signal-to-noise ratio can be observed in Figure 2, starting from offsets (source-receiver distance) ± 6 - 8 km, up to offsets of ± 20 - 25 km, followed by wide-aperture Moho reflection (PmP) and upper mantle refraction (Pn) at the farther offsets. We observe large variations in the amplitude-versus-offset behavior, suggesting strong heterogeneities in the oceanic crust.

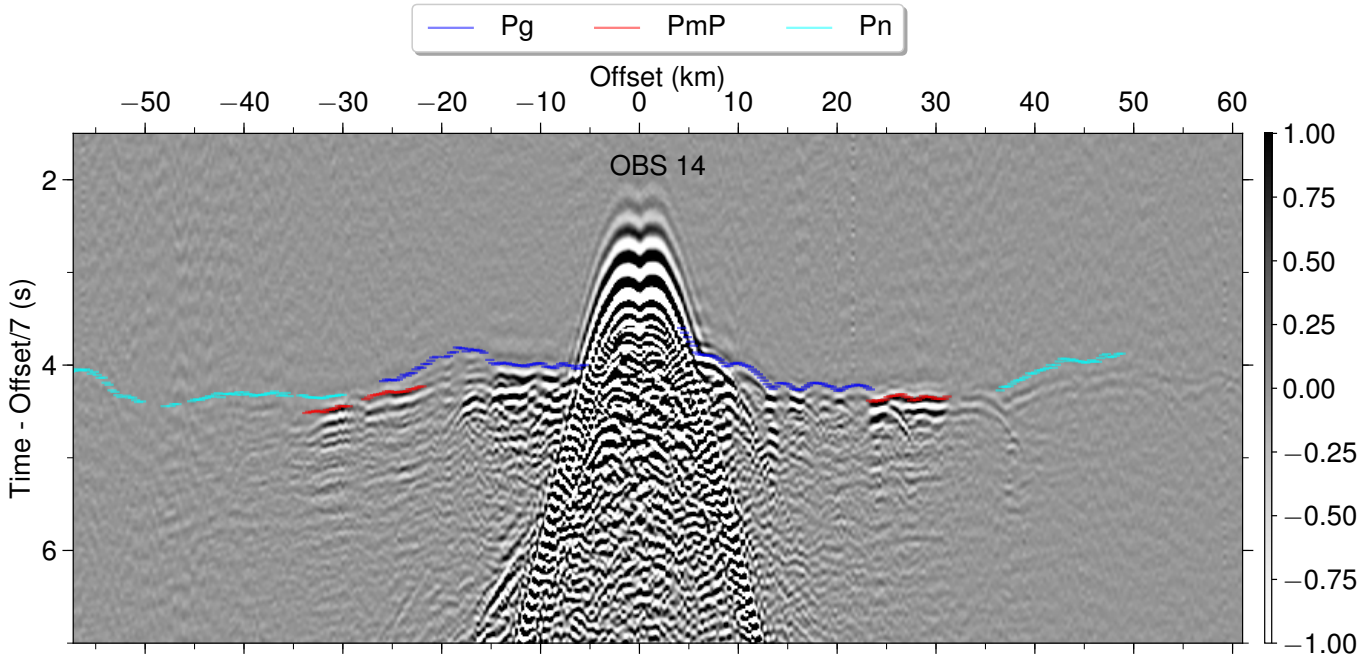

Figure 2. Observed data from OBS 14 after data processing. The blue, red and cyan lines refer to the Pg (crustal turning waves), PmP (Moho reflection) and Pn (Mantle refraction) arrivals. The time was reduced with 7 km/s.

3.2 Travel time tomography

Travel time tomography was used to estimate seismic velocity model of the oceanic crust, using crustal turning waves (Pg) and the wide-angle Moho reflection (PmP) from the boundary between crust. The travel times of the Pg and PmP arrivals were hand picked on the OBS data after bandpass filtering of 4 – 20 Hz, with picking uncertainties of 30-50 ms and 50-70 ms, respectively (Gregory et al., 2021; Wang and Singh, 2022). We used the velocity model from Wang and Singh (2022) as a starting velocity model for FWI.

3.3 FWI

FWI is the current state-of-the-art technique for obtaining high-resolution quantitative subsurface models from seismic data (Tarantola 1984; Shipp & Singh, 2002; Tromp et a., 2005; Fichtner et al., 2006; Virieux & Operto, 2009). Unlike travel-time tomography which only uses the travel time information (Van Avendonk et al., 1998), the FWI is based on minimizing the waveform difference between the observed and synthetically computed seismic data, with a numerical solution of the elastic wave equation for describing the full physics of seismic wave propagation in the solid Earth (Shipp & Singh, 2002).

We adopt a multi-stage strategy for inverting the Pg arrivals in the OBS data for obtaining the oceanic crustal model. In the first stage of FWI, where the tomographic model is used as the starting model, a trace-normalized FWI (Shen, 2010) is applied, with the misfit function defined as

$$J = \sum_{i=1}^{\mathrm{Ns}} \sum_{j=1}^{\mathrm{Nr}} \left\| \frac{\mathbf{s}_{i,j}}{\|\mathbf{s}_{i,j}\|} - \frac{\mathbf{d}_{i,j}}{\|\mathbf{d}_{i,j}\|} \right\|^2, \quad (1)$$

Considering that $\frac{\partial \|\mathbf{s}_{i,j}\|}{\partial \mathbf{s}_{i,j}} = \frac{\mathbf{s}_{i,j}}{\|\mathbf{s}_{i,j}\|}$, the adjoint source is

$$\frac{\partial J}{\partial \mathbf{s}_{i,j}} = \left(\frac{\delta \mathbf{d}_{i,j}}{\|\mathrm{s}_{i,j}\|}\right) - \left(\frac{\delta \mathbf{d}_{i,j}^{T} \cdot \mathbf{d}_{i,j}}{\|\mathrm{s}_{i,j}\|^{2}} \frac{\mathrm{s}_{i,j}}{\|\mathrm{s}_{i,j}\|}\right), \quad (2)$$

where $\mathbf{s}_{i,j}$ and $\mathbf{d}_{i,j}$ are seismic traces (1-D time-series vectors) from the synthetic and field data respectively, $\|\quad\|$ is the *l*-2 norm, i and j are the indexes for the sources and receivers, Ns and Nr are the number of sources and receivers.

This intermediate step is used to bridge the gap between travel-time tomography and the classic FWI using 'true amplitude' waveforms: the influence of amplitude-versus-offset is eliminated in the misfit function and the adjoint source through trace-by-trace normalization, while the amplitude variation along the time axis within each trace remains. This ensures that the waveform inversion will focus more on the phase comparison before moving to explore more waveform amplitude features. In addition, an important aspect of the trace-normalized inversion involves determining the amplitude normalization factors between the synthetic and real data for the OBS gathers as each OBS may has different local amplification due to site or instrument effects.

In the second stage, the output velocity model from trace-normalized FWI is used as the starting model. We perform the classic true-amplitude FWI (Tarantola 1984; Shipp and Singh, 2002), with the misfit function defined as

$$J = \sum_{i=1}^{\mathrm{Ns}} \sum_{j=1}^{\mathrm{Nr}} \left\| \mathbf{s}_{i,j} - \mathbf{d}_{i,j} \right\|^{2}, \quad (3)$$

and the adjoint source is

$$\frac{\partial J}{\partial \mathbf{s}_{i,j}} = \left(\mathbf{s}_{i,j} - \mathbf{d}_{i,j}\right). \quad (4)$$

The waveform misfit functions of FWI in equations 1 and 3, which in this study contains the waveform differences of the observed and synthetically computed crustal P-wave turning waves, can be minimized by iteratively updating the P-wave velocity model of the oceanic crust. Despite different misfit functions, the only difference in the two FWI workflows is the adjoint source (Tromp et a., 2005). The gradient of the misfit function with respect to the P-wave velocity can be efficiently calculated from the zero-lag cross correlation of the source and adjoint wavefields using (Shipp and Singh, 2002)

$$\frac{\partial J}{\partial v_p} = \frac{\rho v_p}{2(\lambda+\mu)^2} \sum_{Ns} (\sigma_{xx} + \sigma_{zz})(\tau_{xx} + \tau_{zz}), \quad (5)$$

where v_p is the P-wave velocity, ρ is the density, λ and μ are the Lamé parameters. σ_{xx} and σ_{zz} are the normal stress components of the source wavefield from forward-time propagation by solving the elastic wave equation in the stress and particle-velocity formulation (Virieux, 1986) with the source wavelet, and τ_{xx} and τ_{zz} are the normal stress components of the adjoint wavefield from backward-time propagation using the adjoint source. The implementation of the cross-correlation operation in equation 5 requires simultaneous access to the stress wavefields at the same propagation time steps between the forward-time source and backward-time adjoint wavefields. We used the boundary value wavefield reconstruction method (Nguyen & McMechan, 2015) to avoid storing the entire history (time-space) of the source wavefield either in the memory or in the hard disk. The price is one additional wavefield propagation simulation that is feasible with the modern computing facilities.

The S-wave velocity model was derived from the P-wave velocity using Brocher (2005)'s regression fit. Density was linked to the P-wave velocity based on the empirical relation of Hamilton (1978) for velocity smaller than 2.2 km/s, and the Gardner et al. (1974)'s relation for higher velocities. We used the time-domain staggered-grid finite-difference method (Virieux, 1984) with fourth-order spatial and second-order temporal accuracy for solving the elastic wave equation. The grid spacing for the finite-difference was 20 m in both the horizontal (distance) and vertical (depth) directions. The time step was 0.0012 s. We applied the convolutional perfectly matched layer absorbing boundary condition (Komatitsch & Martin, 2007) at the model boundaries. Considering the sparse distribution of OBSs, a Gaussian smoothing operator with 4 km horizontal and 0.4 km vertical lengths (Guo et al., 2022) was applied to the gradient model for regularization. The model update was further conditioned using the conjugate-gradient method for defining the search direction for minimizing the misfit functions. The step length for model update was estimated from a line search along the gradient direction using a parabolic fit (Vigh & Starr, 2008).

3.4 Data selection

For the inversion, we used the pressure component of the crustal turning waves (Pg), because the Pg arrivals have the most linear behaviour with regard to the P-wave velocities of the oceanic crust. Moho reflections (PmP) were not used in the FWI for constraining the velocity model, because of its strong nonlinearity around the critical angles (Guo et al., 2021). A time-window of 0.7 s was applied to the OBS gathers, by muting the data before 0.3 s and after 0.4 s of the picked Pg travel times, to reduce the influence of noise and to isolate the Pg arrivals from the

other seismic events. Throughout the FWI, we excluded the Pg arrivals with offsets smaller than 5 km because of the potential interferences with the strong seafloor reflections.

The inversion was carried out by first inverting for the near-to-intermediate source-receiver offset data (from ± 5-8 km up to ±15 km offsets) followed by including the Pg waveforms from the farther offsets (up to ±20 - 25 km offsets). The workflow effectively updates the P-wave crustal model from shallower to deeper depth, because turning waves of smaller offsets propagate in the shallower oceanic crust. The updated velocity model from the prior stage was used as the starting model for the next stage of inversion. Since the number of the shots is considerably larger than the number of the receivers for an OBS seismic survey, we used reciprocity for switching the locations of the sources and receivers for an efficient seismic wave modeling while maintaining the same accuracy (Operto et al., 2006). The explosive sources were applied to the OBS locations at the seafloor for the normal stress components. The simulated data of pressure wavefield can be obtained from the average of the normal stress components at the original shot positions.

3.5 Source wavelet estimation

Solving the elastic wave equation requires the source wavelet as an input. The direct water waves from the air-gun array at the sea surface tend to overlap with the strong scatterings/reflections from the rugged seafloor and reflections from the basement, therefore it can be challenging to obtain a reliable source signature directly from the water waves. Here we compare two methods for estimating the source wavelet. First, we estimate the source wavelet by aligning and stacking the near-offset crustal Pg arrivals from 5 km to 7 km, because the Pg waves do not interfere with the subsurface reflectors and thus preserve the original source signature. Figure 3a shows the

316 selected crustal Pg waves from the near offsets (dashed grey lines and solid black lines, before
317 and after aligning) of OBS 15 in the frequency band of 3 – 10 Hz. We stacked the aligned
318 waveforms to enhance the signal to noise ratio, and the output is the estimated source wavelet
319 (solid green line in Figure 3a).

320 Alternatively, we can extract the wavelet signature from the near-offset free-surface multiples.
321 We observe a good isolation of the direct waves in their free-surface related multiples (Guo et
322 al., 2021) in the frequency band of 3 – 40 Hz, possibly because the strong seafloor-related
323 scatterings in the primary arrivals have been dispersed during the two-way wave propagation in
324 the seawater. Figure 3b shows the free-surface multiples (dashed gray lines) between the offsets
325 of -1 km and 1 km, from 10.3 to 10.7 s. The waves have been aligned, as shown by the solid
326 black lines. Similarly, we stacked the aligned waves to obtain the source wavelet (solid green
327 line in Figure 3b).

328 Finally, we filtered the two estimated source wavelets, from the Pg arrivals and the free-surface
329 multiples, respectively, into the same frequency range of 3-10 Hz. Figure 4 illustrates the
330 comparison of the wavelets from the two different parts of the data, which reveals remarkably
331 consistent source signatures.

332 We used the obtained source wavelet from free-surface multiples (Figure 4, dashed red line) for
333 seismic full waveform modeling using the elastic wave equation. The velocity model is from
334 travel-time tomography (Wang and Singh, 2022). Figure 5a and 5b show the comparison of the
335 simulated and field data for OBS 15 and OBS 20, respectively, at near offsets. The good
336 waveform matches in Figure 5 suggest that the estimated source wavelet in Figure 4 provides a
337 reliable approximation to the original source signature during the OBS data acquisition. Note that

in Figure 5, the synthetic data has been normalized, and shifted along the time axis to align with the field data, in order to focus the comparison on the shape of the waveforms. We estimated the amplitude scaling factors for each OBS gathers from the ratio of the l-2 norm of the field and synthetic data.

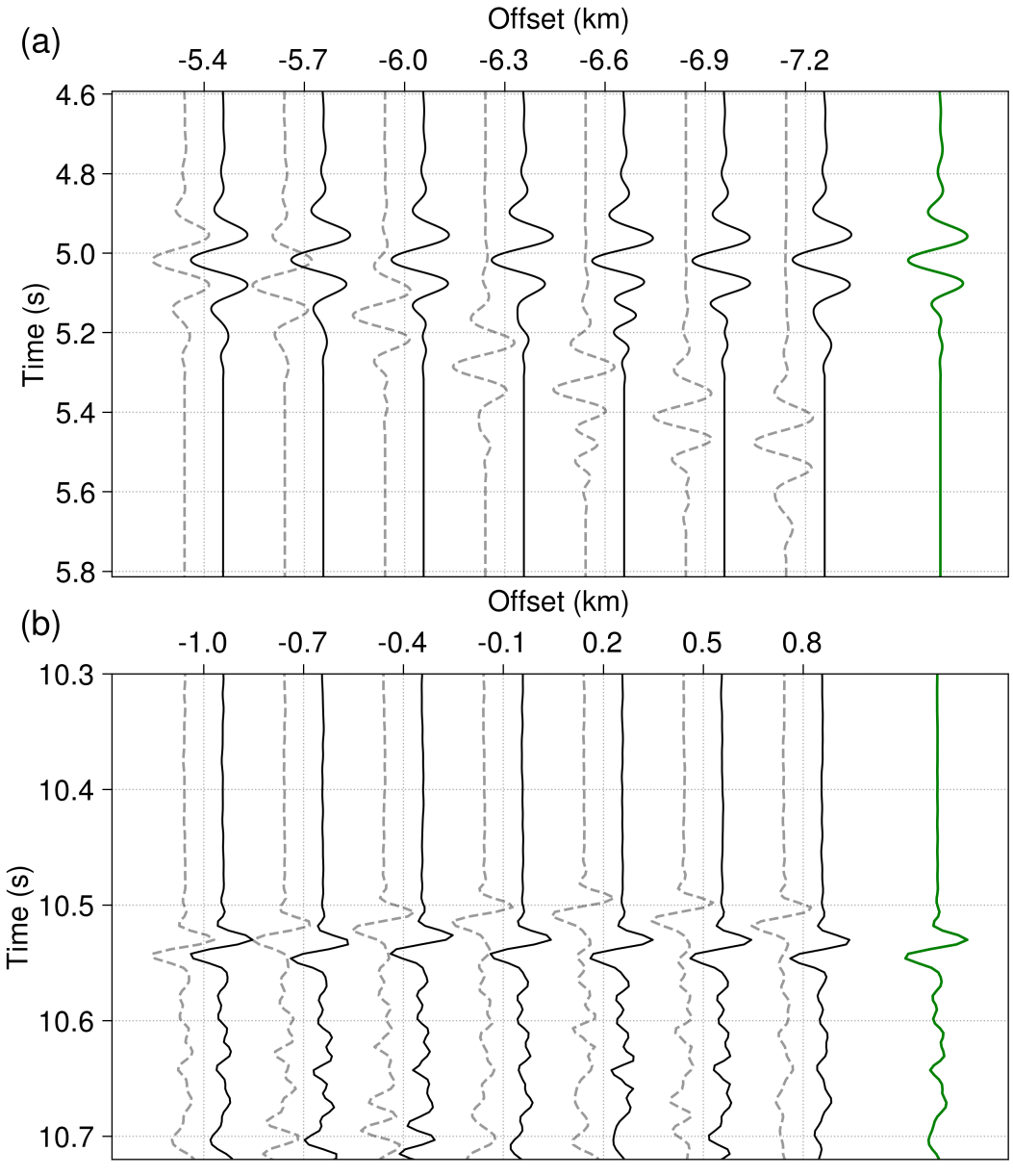

343 **Figure 3.** Source wavelet estimation from near-offset Pg arrivals and free-surface multiples. (a)
344 shows the near-offset Pg arrivals before (dashed grey lines) and after (solid black lines) aligning,
345 in the frequency range 3 – 10 Hz. Solid green curve shows the stacking result. (b) shows the free-
346 surface multiples between -1 and 1 km offsets before (dashed grey lines) and after (solid black
347 lines) alignment, in the frequency range 3 – 40 Hz. Solid green curve shows the stacking result.

348

349

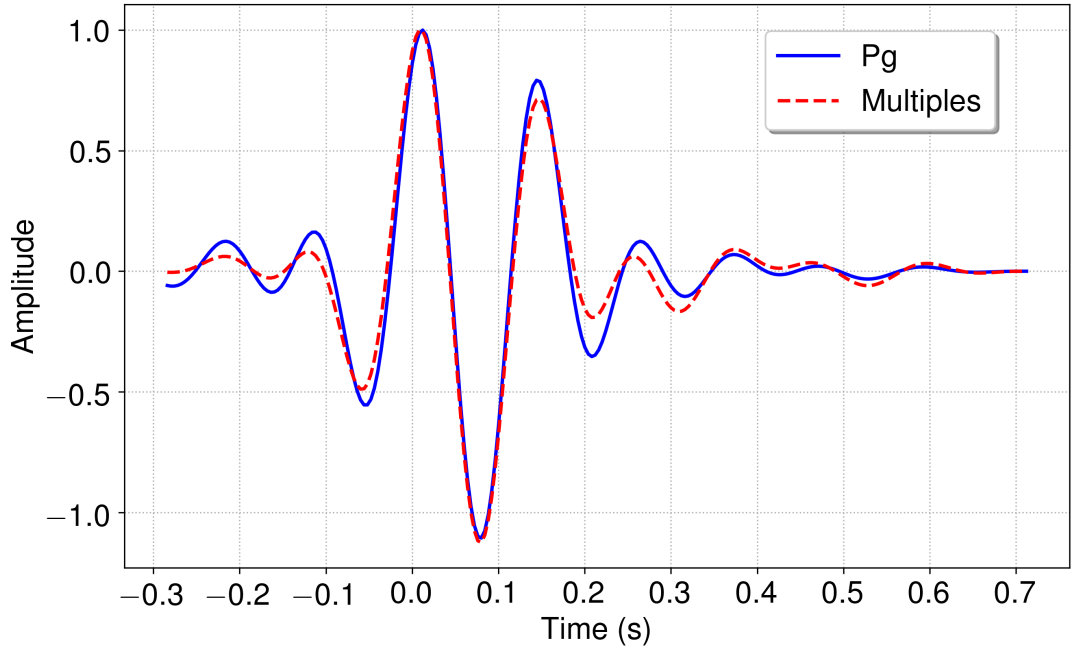

350

351 **Figure 4.** Comparison between the extracted source wavelets from Pg and free-surface multiples
352 of water waves, in the frequency range of 3 – 10 Hz.

353

354

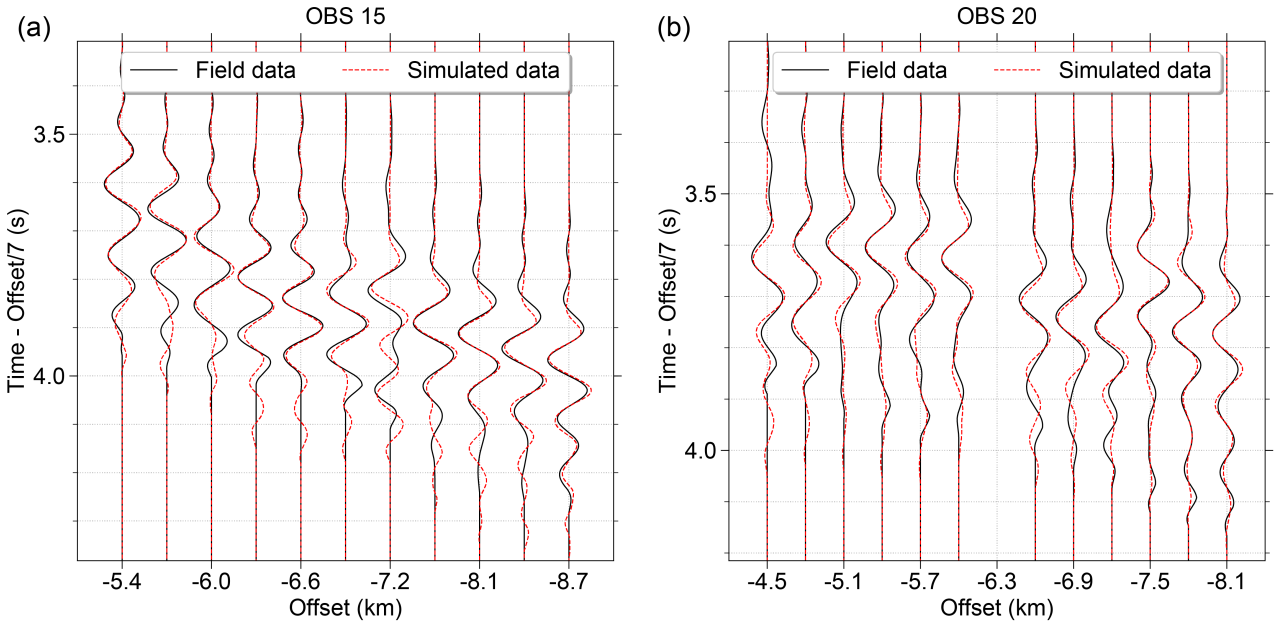

Figure 5. The comparison between the Pg arrivals of the field and synthetic data at the near offsets for OBS 15 and OBS 20, respectively. Note that the synthetic data has been aligned with the field data to focus the comparison on the shape of the waveforms.

4 Results

4.1 Data misfit and waveform comparison from FWI

As mentioned before, we used a two-stage hierarchy inversion approach, starting with a trace-normalized FWI followed by the classic true-amplitude FWI. For different FWI stages, the inversion first inverted for the near-to-intermediate offsets of data, followed by using the full range of Pg arrivals. Each inversion step contains 20 iterations, which leads to 80 iterations in total. Figure 6a shows the data misfits for all the 80 iterations from the trace-normalized and the true-amplitude FWI. Figure 6b shows the data misfits for each of the 9 OBS gathers from the

369 tomographic and the final FWI models. The data misfits have been reduced substantially after
370 the FWI for each of the OBS gather.

371 Figure 7 shows the observed and simulated seismic waveform data from OBS 15. The simulated
372 seismic data after the FWI show a much better match to the crustal Pg arrivals in the field OBS
373 data than those from the tomographic model, suggesting that the FWI method has improved the
374 crustal velocity model.

375

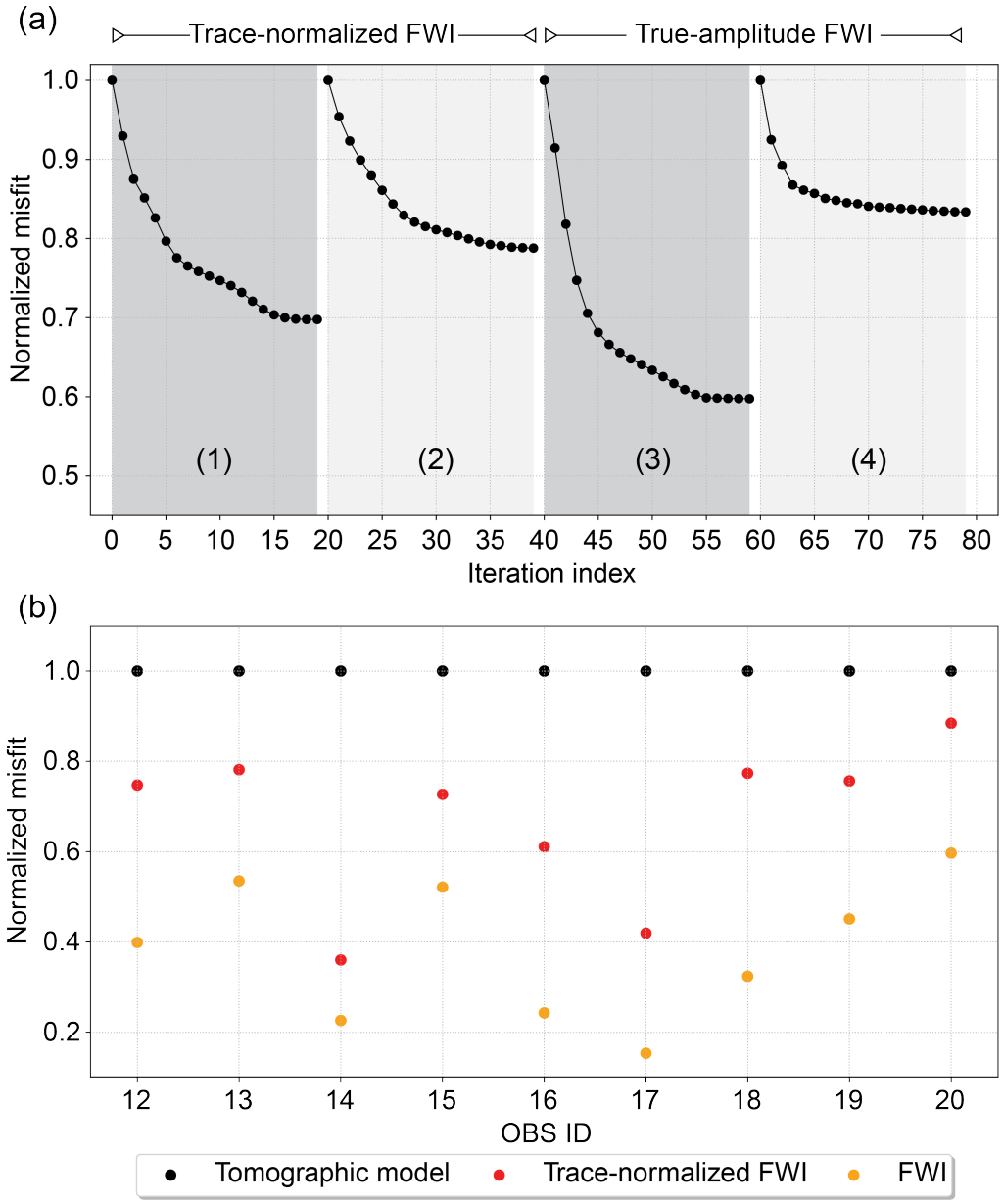

Figure 6. Data misfits from FWI. (a) The misfits as a function of iteration indexes come from the trace-normalized FWI of the near-to-intermediate (iterations 1-20) and full (iterations 21-40) offsets, and true-amplitude FWI of the near-to-intermediate (iterations 41-60) and full (iterations 61-80) offsets. Each inversion, as indicated by different background colors, contains 20 iterations. (1) and (3) use near-to-intermediate offset Pg waves and (2) and (4) use all (full offset range) the Pg arrivals in the OBS data. Note that the misfit was normalized to 1 at the beginning

of each inversion step for plotting purpose. (b) Data misfit for each of the 9 OBS gathers from the tomographic and the final FWI models. The waveform data misfits were calculated using equation 3.

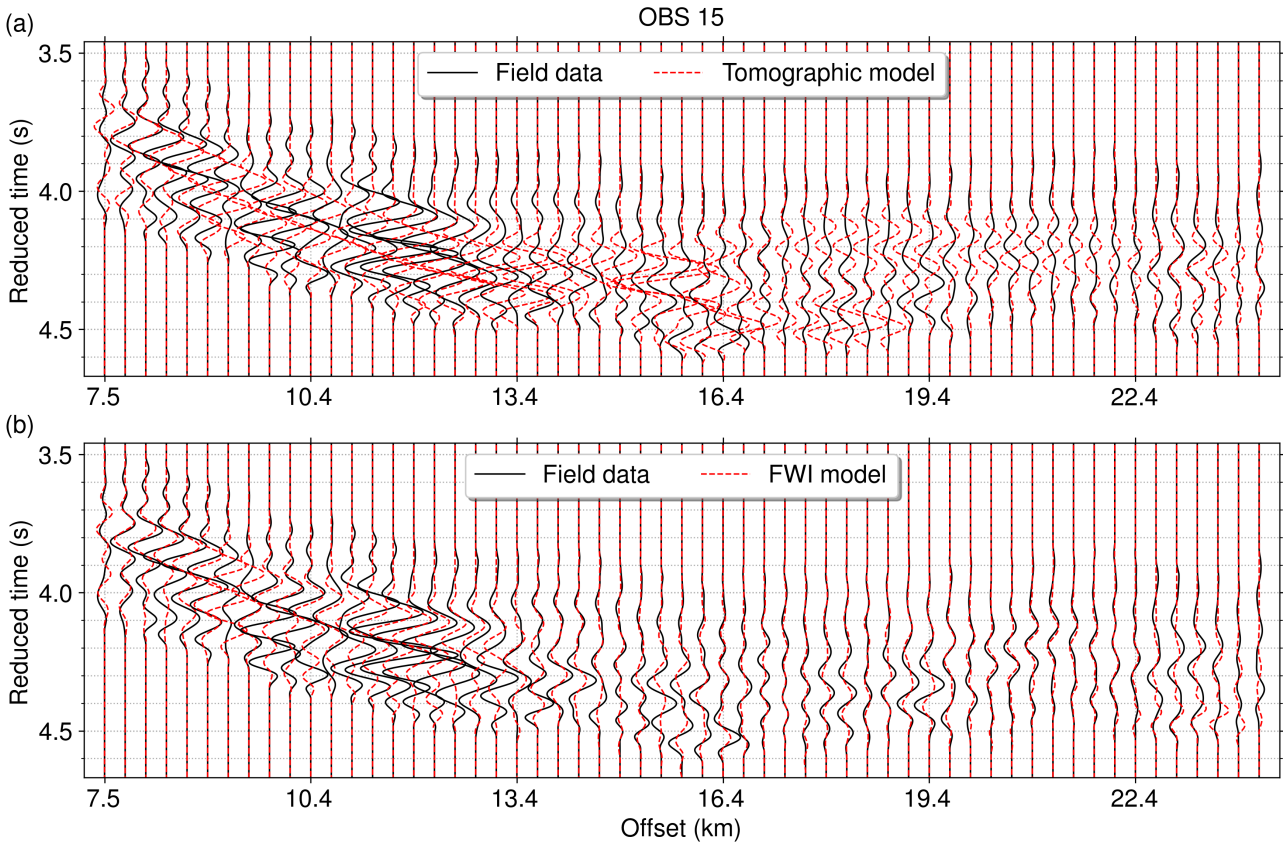

Figure 7. Observed and simulated seismic waveform data from OBS 15. (a) The field data (black) and the synthetic waveform (red) using the tomographic model. (b) The field data (black) and the synthetic waveform (red) after 80 iterations of the FWI. The travel time was reduced with a velocity of 7 km/s for both the field and simulated data.

394

395 **4.2 Oceanic crustal models from FWI**

396 Figure 8a shows the P-wave velocity model from travel-time tomography, which provides a very
397 good travel-time fit for the first arrivals (Wang and Singh, 2022). Since the travel time is mainly
398 sensitive to large-scale velocity structures, the tomographic velocity model contains few details
399 in the oceanic crust but clearly shows velocity of 5 to 6.5 km/s in the upper crust and the velocity
400 of 6.6 - 7 km/s in the lower crust. Travel-time tomography suggests that the crustal thickness is
401 nearly uniform (5.6±0.2 km) along the whole profile (Wang and Singh, 2022).

402 Starting from the travel-time tomographic velocity model (Figure 8a), we proceeded with a
403 sequential application of the trace-normalized FWI and the classic true-amplitude FWI methods.
404 The crustal velocity model from trace-normalized FWI contains intermediate-scale features
405 (Figure 8b). Figure 8c presents the final oceanic crustal velocity model with fine-scale geological
406 features from the classic true-amplitude FWI. The FWI-derived velocity models (Figures 8b and
407 8c) delineate the oceanic crust with a higher resolution than that from the travel-time tomography
408 (Figure 8a). We observe strong heterogeneities in the oceanic crustal model (Figure 8c).

409 We plot the high-resolution seafloor bathymetry data surrounding the OBS profile in Figure 9a.
410 To highlight the salient features of the final crustal models from FWI, in addition to the velocity
411 model in Figure 9b (the same with Figure 8c), we also show the velocity anomaly model (the
412 difference between the final velocity model from FWI and that from the travel-time tomography)
413 (Figure 9c), the vertical velocity gradient (Figure 9d), which is the derivative of FWI-derived
414 velocity model with respect to depth (the z direction), and the horizontal velocity gradient (the
415 derivative of FWI-derived velocity model along the distance direction) (Figure 9e). Compared
416 with the tomographic P-wave velocity model (Figure 8a), we observe a generally positive

velocity anomaly in the shallow crust and an overall negative velocity anomaly at the greater depths (Figure 9c), similar to a recent study near the Mid-Atlantic Ridge (Guo et al., 2022), albeit Figure 9c contains more variations. The vertical velocity gradient in Figure 9d in the shallow crust is in general larger than that at the greater depths. The complicated positive and negative patterns in the horizontal velocity gradient (Figure 9e) highlights the strong lateral crustal heterogeneities in the region.

4.3 Heterogeneous oceanic crust: seafloor morphology and distinct crustal segments

From the high-resolution seafloor bathymetry in Figure 9a, we can discern four distinct features, each spanning 20-30 km in distance. From north to south, firstly, we observe linear features in proximity to OBS 14 and OBS 12, which are parts of the St Paul FZ. Moving further south, we encounter an abyssal hill morphology, followed by a notable sediment layer with a thickness reaching up to 1.5 km and a remarkable basement topography. Lastly, on the leftmost side, a landslide surface becomes evident, which is associated with the northern flank of the Romanche TF. These four zones are defined as zone 1 to 4.

Correspondingly, we discover four distinct crustal segments in the velocity model within the ~120 km long section (Figure 9b) associated with the overlying seafloor bathymetry. From right to left in Figure 9b, the segment affected by the St. Paul FZ is characterized with features of a three-layered (normal) oceanic crust, which includes a ~2-km thick layer where the velocity increases from ~ 4.8 to 6 km/s (separated by a dashed white line), a 1.5-km thick middle crust with reduced vertical velocity gradient with a velocity of 6-6.5 km/s, which is underlain by high velocity ~6.6 – 7.0 km/s (top boundary indicated by the solid white line) in the lower crust. The

base of the uppermost crust is marked by a change in the vertical velocity gradient, but it is deeper than a normal layer 2A/2Bboundary (Audhkhasi and Singh, 2019), which might represent the layer 2/3 boundary (Guo et al., 2022). The reduced velocity of 6-6.5 km/s in the middle crust might be due to the presence of fractures associated with the St Paul FZ. In the lowest layer, the velocity (6.5-7.0 km/s) is typical of lower crustal velocity. Zone 2, the segments associated with the abyssal hill morphology, consists of only two layers, ~2-2.5 km thick upper crust and a high velocity ~7 km/s zone with a thickness at least ~3.5 km. Zone 3, the segment from distance 520 km to ~545 km associated with the low basement morphology, seems to have velocities of 5.5 – 6 km/s starting near the basement extending down to 4 km depth with subtle variations. Finally, in zone 4 with a landslide topography on the seafloor, the leftmost segment shows a three-layer structure of a normal oceanic crust. The top layer has a high vertical velocity gradient, underlain by a layer with velocity from ~6 km/s and intermediate velocity gradient, and a bottom layer with high velocity starting from 6.5 km/s and low velocity gradient.

Figure 10 shows four selected one-dimensional (1-D) velocity-depth profiles below the basement from the four zones from the tomographic (Figure 8a) and FWI (Figure 8c) models. Comparing the 1-D velocity profiles across different locations clearly show the strong heterogeneities in the crust, albeit there are more velocity variations both vertically and horizontally in the FWI model. The 1-D velocity in Figures 10a is from zone 1, containing three-layer oceanic crust. Figure 10b shows velocity profile from zone 2, with 7 km/s velocity appears at 2.4 km depth from the basement. Figure 10c shows the velocity-depth profiles from zone 3. Contrary to a normal oceanic crust, we observe subtle variations with depths, with smaller vertical velocity gradients. The velocity profiles have a velocity near to 5.5 - 6 km/s in the vicinity of basement. The P-wave velocity in Figure 10d from zone 4 contains features of a normal oceanic crust. The top layer

462 down to ~ 1 km depth has a high velocity gradient, possibly layer 2A (Audhkhasi and Singh,
463 2019), and is underlain by a layer with intermediate velocity gradient (layer 2B). From ~2.5 km
464 below the basement, the velocity is 6.5 – 7 km/s with small velocity gradient, associated with
465 high velocities in the lower crust.

466

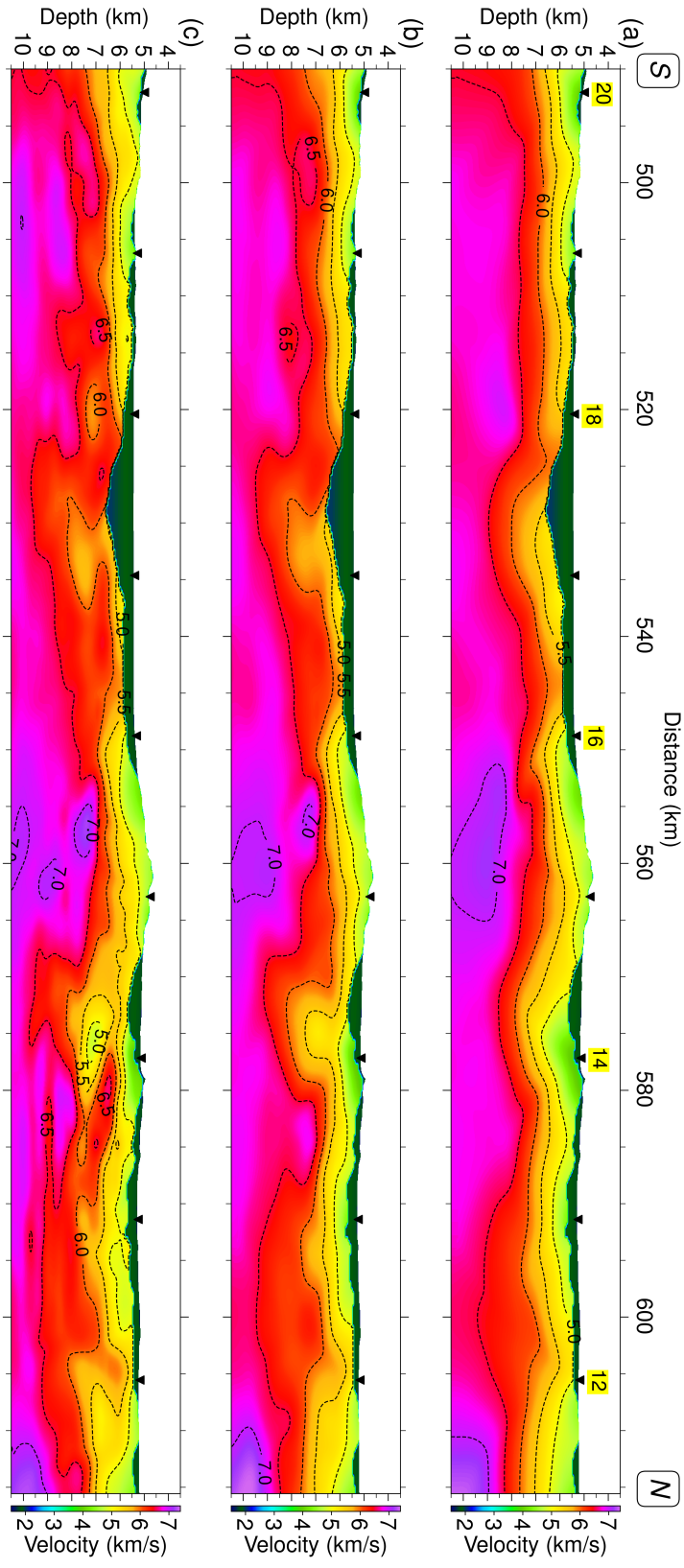
(a)
(b)
(c)
S
N
Depth (km)
Distance (km)
Velocity (km/s)
20
18
16
14
12
500
520
540
560
580
600
6.0
6.5
7.0
5.0
5.5

Figure 8. Seismic P-wave velocity models over a 120 km-long section between the St Paul fracture zone (FZ) and the Romanche transform fault (TF). (a) The velocity model from travel-time tomography, (b) the velocity model from the trace-normalized FWI, and (c) the final velocity model from the classic true-amplitude FWI. Black triangles at the seafloor mark the OBS locations, with the associated OBS IDs labeled in (a). The velocity contours of dashed black lines are from 5 to 7 km/s with an increment of 0.5 km/s. Distance 0 along the profile is at the location of extended 6 km from the lower end of the shot profile in Figure 1b, with the longitude and latitude of (-16.9855, -3.65597) (Wang and Singh, 2022). The labels of 'N' and 'S' at top of (a) indicate the north and south directions.

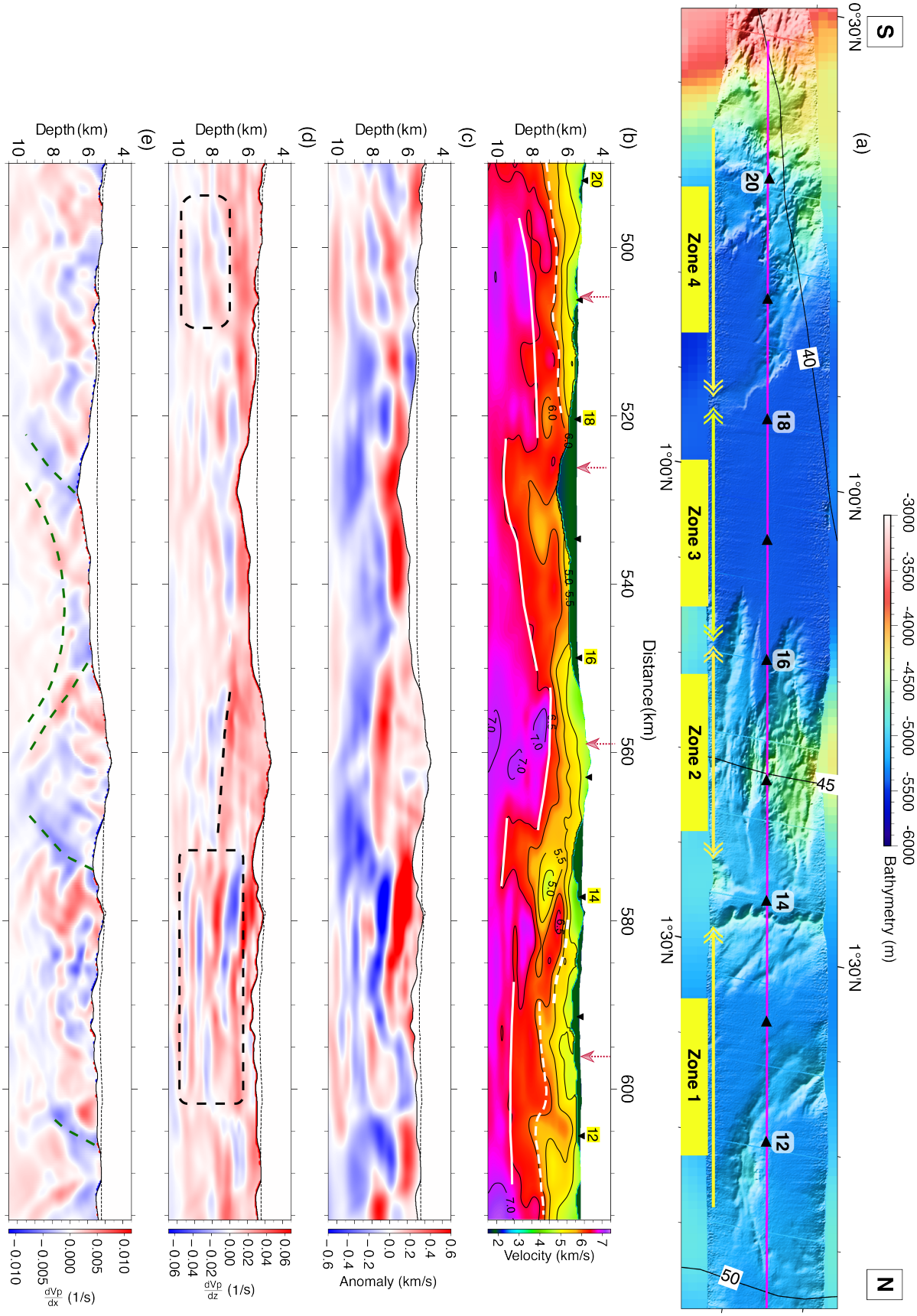
S
N
0°30'N
1°00'N
1°30'N
18°12'W
18°06'W
Zone 4
Zone 3
Zone 2
Zone 1
Bathymetry (m)
-3000
-3500
-4000
-4500
-5000
-5500
-6000
(a)
(b)
(c)
(d)
(e)
Distance(km)
Depth (km)
Velocity (km/s)
Anomaly (km/s)
$\frac{dVp}{dx}$ (1/s)
$\frac{dVp}{dz}$ (1/s)

Figure 9. FWI-derived oceanic crustal models along the seafloor bathymetry. (a) The high-resolution seafloor bathymetry along the OBS profile between the St. Paul FZ and the Romanche TF. Black triangles at the seafloor mark the OBS locations, with the associated OBS IDs labelled. The pink line shows the source locations for the survey. The plate ages were plotted using black lines and labelled every 5 Myr (Müller et al., 2008). (b) The final P-wave velocity from FWI (the same with Figure 8c). Black triangles at the seafloor mark the OBS locations, with the OBS IDs labelled. The velocity contours of dashed black lines are from 5 to 7 km/s with an increment of 0.5 km/s. The dashed white lines in zones 1 and 4 mark the vertical velocity gradient changes. The solid white line generally traces the 6.5 km/s contour, indicating the top boundary for high velocities ~7 km/s. (c) The velocity anomaly, the difference between the velocity models from FWI and travel-time tomography. (d) The vertical velocity gradient, the derivative of the velocity model with respect to depth (z direction). (e) The horizontal velocity gradient, the derivative of the velocity model with respect to the distance (x direction). The dashed red arrows mark the locations for the 1D profiles in Figure 10. The labels of 'N' and 'S' at top of (a) indicate the north and south directions. The dashed lines and rectangles in (c) to (e) are discussed in the discussion section.

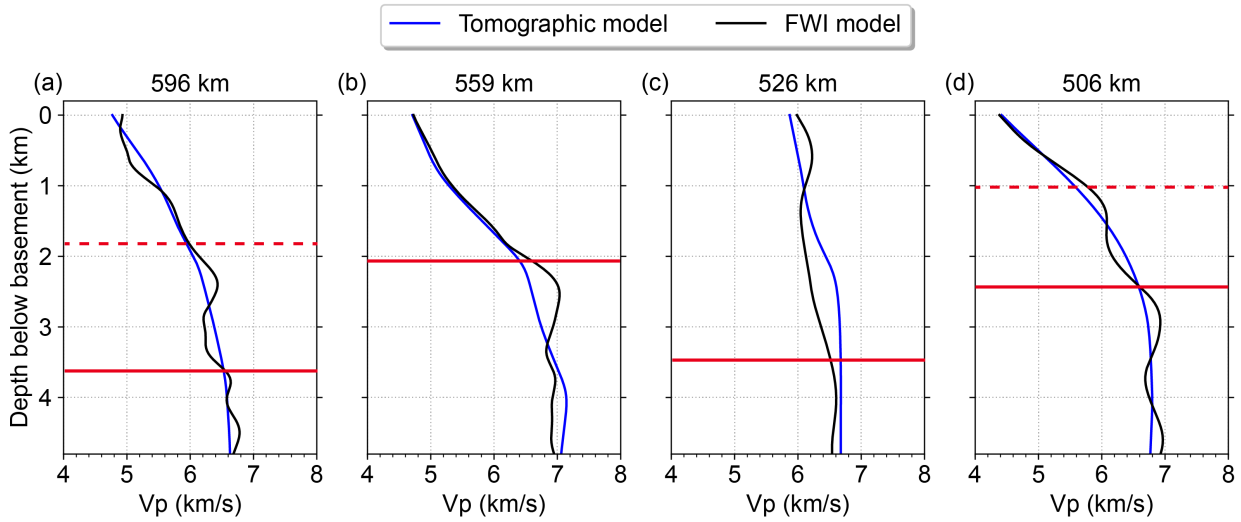

Figure 10. Velocity-depth (1-D) profiles from different distances along the profile in the seismic P-wave velocity models for the oceanic crust. The solid blue curves are from the travel-time tomographic model (Figure 8a), and the solid black curves are from the FWI model (Figure 8c). The dashed horizontal lines indicate the boundary for vertical velocity gradient changes, and the solid horizontal lines indicate the top boundary of high velocities.

4.4 Sensitivity and resolution tests

To demonstrate that the Pg waveform from the wide-angle OBS data has the capability for resolving the scale of oceanic crustal heterogeneity that we observe in Figure 9, we performed checkerboard tests for estimating the size of the anomaly that can be recovered by the FWI of crustal turning waves. When performing synthetic forward modelling and FWI, we used the same source and receiver positions and frequency ranges of the data as in the actual observation,

524 and the same inversion parameters. The same data windowing was applied using Pg travel-time
525 picks from the field data.

526

527 We generated synthetic models by adding 5% positive and negative Gaussian-shaped velocity
528 anomalies to the tomographic velocity model (Figure 8a). The anomalies have sizes of 10 km in
529 length and 1 km in thickness for one case (Figure 11a), and 10 km in length and 0.5 km in
530 thickness for the other case (Figure 12a). We computed the 'Observed' data using the perturbed
531 velocity model. The FWI started from the unperturbed tomographic model to see how well these
532 perturbations can be recovered. After the FWI, the anomalies are well resolved and exhibit a
533 good match to the true models (Figures 11 and 12). In Figure 12 where the anomalies are
534 smaller, the estimated anomalies from the FWI still provide a favorable match to the true model,
535 although their accuracy is relatively less well constrained in the area of rough basement
536 morphology. The data also has less resolution for the anomalies in the lower part of the model.

537

538 In order to make sure that some of anomalies are required by data, we removed some of these
539 anomalies in the FWI model to compare the waveform match. For the model section in zone 2
540 (Figure 13), we observe that the waveform match between field data and synthetic data
541 deteriorates when we eliminate the positive and negative velocity anomalies introduced by the
542 FWI. This observation suggests that the anomalies are essential in explaining the strong
543 amplitude variations with offsets. In zone 3 where there are high velocities 5.5 to 6 km/s near the
544 basement, we removed the positive anomalies introduced by the FWI, as shown in Figure 14.
545 Synthetic waveforms were then simulated using the modified model. We notice that the
546 waveform fit to the field data becomes unfavorable when compared with those from the

unaltered FWI model. These tests demonstrate that the introduced anomalies by the FWI are required by the data.

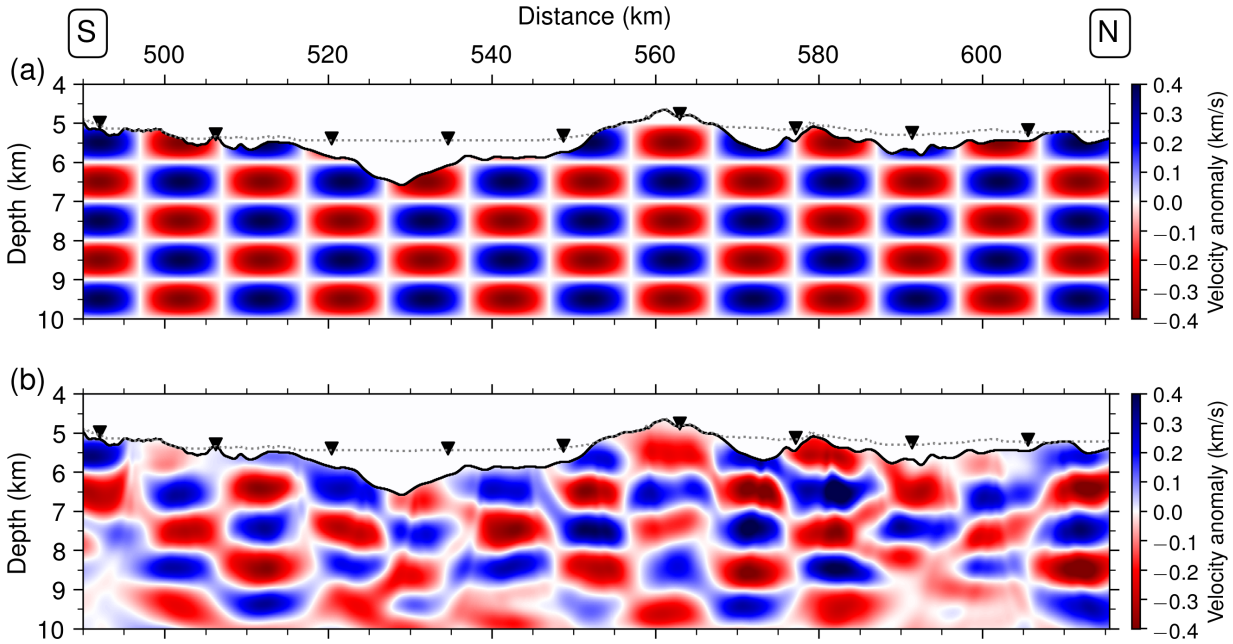

Figure 11. Checkerboard test 1. Each of the anomalies has 10 km lateral extension and 1 km thickness. (a) The true checkerboard velocity perturbation added to the tomographic model, and (b) the recovered velocity anomalies from the FWI. The dashed and solid black lines at top indicate the seafloor and the basement (the top of layer 2), respectively.

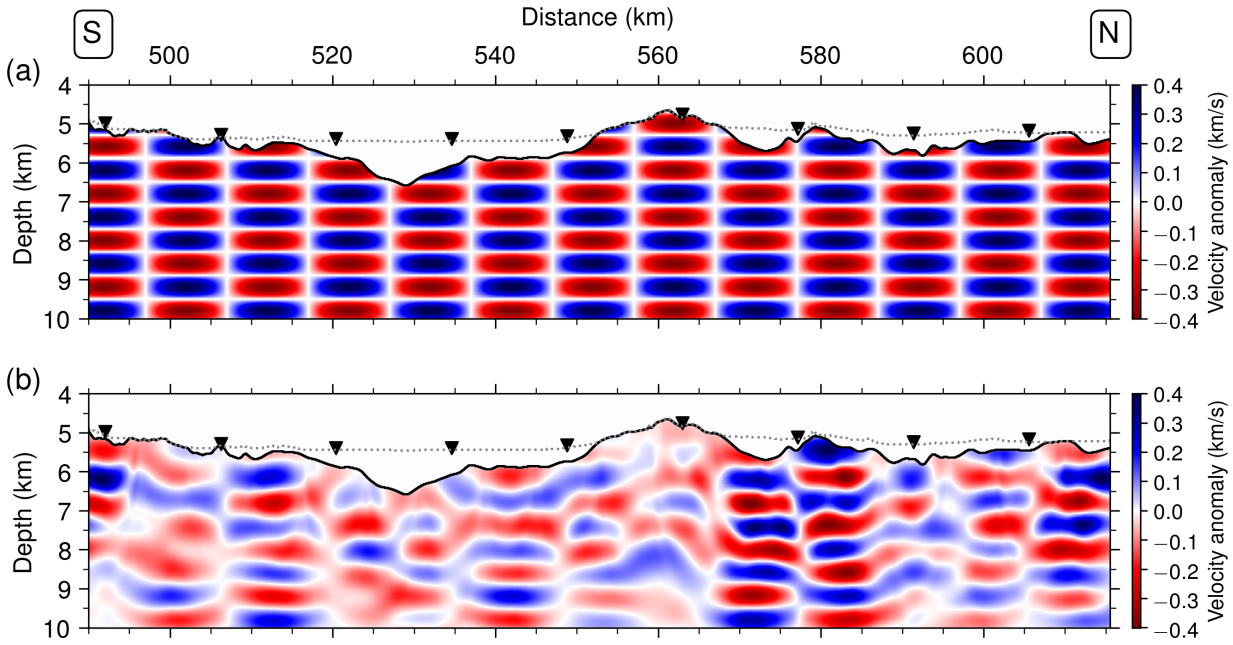

Figure 12. Checkerboard test 2. Each of the anomalies has 10 km lateral extension and 0.5 km thickness. (a) The true checkerboard velocity perturbation added to the tomographic model, and (b) the recovered velocity anomalies from the FWI. The dashed and solid black lines at top indicate the seafloor and the basement (the top of layer 2), respectively.

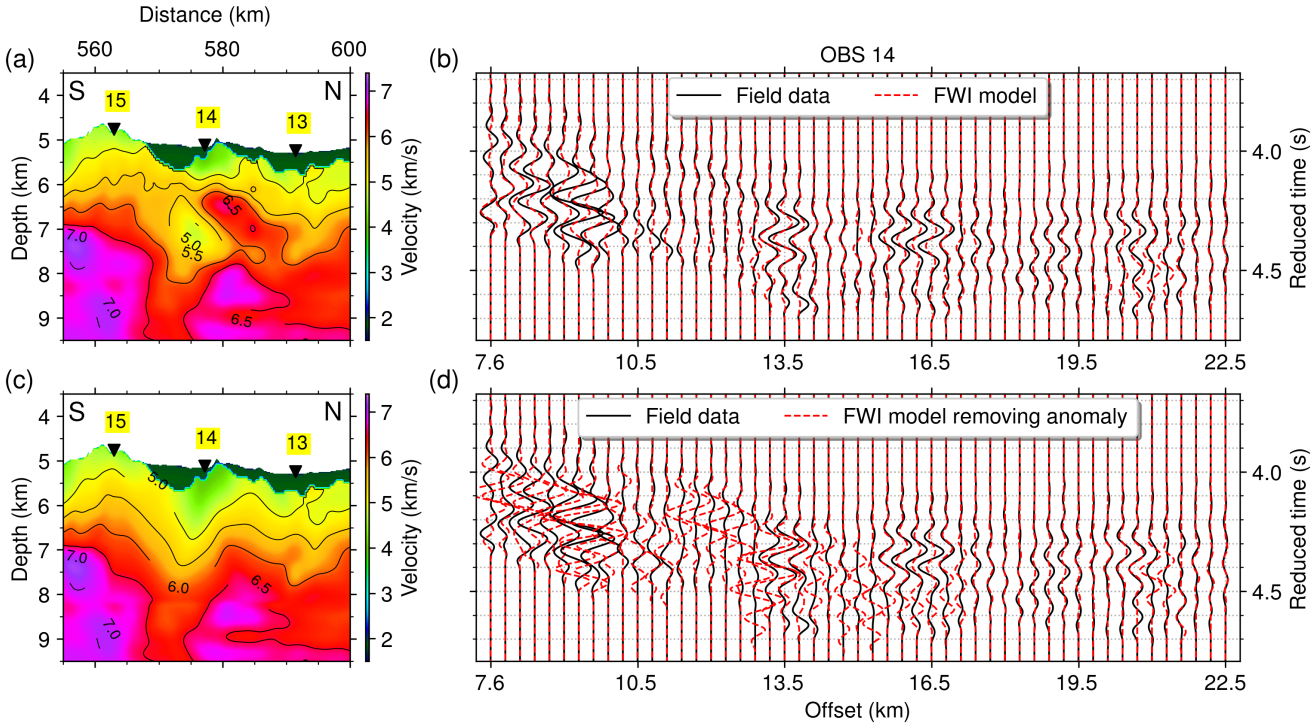

Figure 13. Data comparison after removing the positive and negative velocity anomalies near OBS 14. (a) and (c) show part of the FWI model (Figure 9b) and the model after removing anomalies near OBS 14, the possible faulting structure. (b) shows waveform comparison of field and synthetic data using the FWI model. (d) shows waveform comparison of field and synthetic data using the modified model after removing anomalies.

583

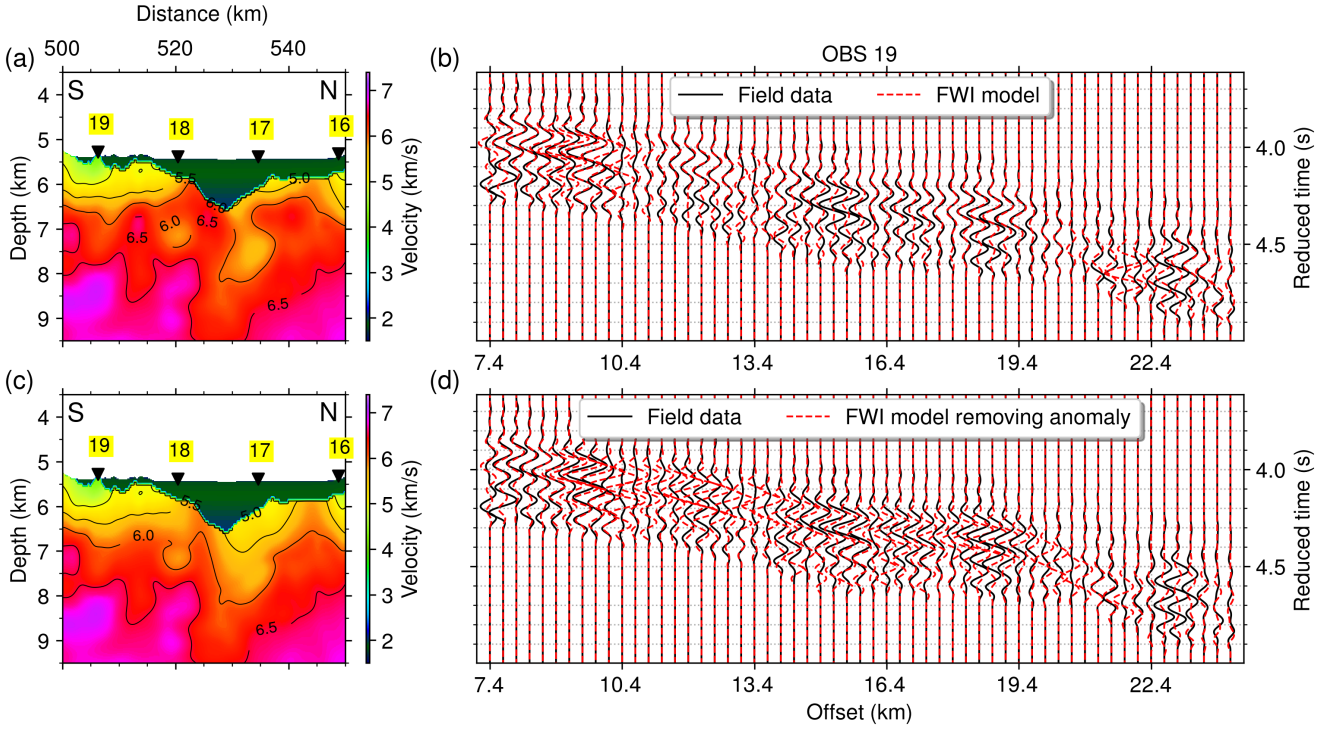

584

585 **Figure 14.** Data comparison after removing the positive velocity anomalies. (a) and (c) show
586 part of the FWI model (Figure 9b) and the model after removing the positive velocity anomalies.
587 (b) shows waveform comparison of field and synthetic data using the FWI model. (d) shows
588 waveform comparison of field and synthetic data using the modified model.

589

590

591 **5 Discussion**

592 Resolution study indicates that FWI of OBS data can resolve structures on the scale of 10 km
593 laterally, and 500-1000 m vertically. Therefore, we will only discuss features of these scales. The
594 velocity anomaly plot (Figure 9c) indicates that there has been ±600 m/s change in velocity from
595 the tomography results. The velocity anomaly also shows the presence of some sub-horizontal

features, especially in zone 1, which becomes more pronounced in the vertical velocity gradient (Figure 9d), as indicated by the dashed rectangles. Although the horizontal velocity gradient is more complex, it does delineate the boundaries between different zones, as marked by the dashed green lines in Figure 9e. Below, we will discuss the underlying accretion mechanisms for the four distinct segments.

5.1 Zone 1

At the right side of the model section (Figure 9b), where the oceanic crust is affected by the St Paul FZ, the observed velocity model shows three-layered oceanic crustal velocities, demonstrating a dominating magmatic process for the crustal formation. The rugged velocity contours in the upper crust could be introduced by the tectonic processes associated with the St Paul FZ. For example, the velocity anomaly around OBS 12 corresponds to the linear feature in the fracture zone illustrated in Figure 9a. The relatively slow seismic velocity suggests highly fractured upper crust affected by the St Paul FZ. The vertical gradient changes, as marked by the dashed white line, could be related to the transition from highly fractured crust to less fractured crust. We observe a low velocity layer between 2.8-3.4 km depths from the basement (Figure 10a), which could be related to enhanced hydrothermal alteration, as having been observed from seismic studies and IODP drilling (Singh et al., 1999; Guo et al., 2022; Wilson et al., 2006). The magmatic origin of crust is consistent with the travel-time tomographic results of Growe et al. (2021), Gregory et al. (2021) and Marjanovic et al (2020), for the St. Paul fracture zone, Romanche transform fault, and the Chain fracture zone, respectively. Our results, however, show more detailed structures in the crust. We also observe layered structures between 1.8 - 4 km depth (indicated by the dashed rectangle in Figure 9d). Guo et al. (2022) found similar structures for 7-12 Ma old crust further south, and interpreted them to be due to the presence of high and

low velocity layers associated with in situ melt injection and crystallization in the lower crust. What is interesting here is that such a layering is observed in a zone affected by the St Paul fracture zone. However, if this sub-segment was formed at a small ridge segment within the transform zone (Maia et al., 2016), and if the lithosphere beneath the transform fault is thin (Wang et al., 2022), there might be enhanced magma supply at inter-transform ridge segment with an increase in melt production due to water-induced melting (Wang et al., 2022).

5.2 Zone 2

Underlying the abyssal hill morphology, both the tomographic and FWI velocity models show the presence of higher velocities compared with surrounding regions. The change of vertical velocity gradient, marked by the dashed black line in zone 2 (Figure 9d), is consistent with the the top boundary of high velocities (solid white line, Figure 9b). The occurance of a high velocity (6.8 – 7 km/s) of at least ~3.5 km thickness, starting at a shallow depth, 2 – 2.5 km from the basement and, is probably related to either due to the presence of serpentinized peridotite or unaltered gabbro rich in olivine (Ol)/clinopyroxene (Cpx). At slow-spreading ridges, long-lived, low-angle detachment faults have been observed that can uplift lower crustal gabbro and mantle peridotite to the shallower crust and the seafloor (Cann et al., 1997; MacLeod et al., 2002; Escartín et al., 2017). For example, seismic surveys in the Kane oceanic core complex (OCC) of the Atlantic Ocean have imaged the distribution of gabbro, serpentinized peridotite and basalt, with a ~1 km thick gabbroic core underlain by a low-velocity peridotite layer (Canales, 2010). Depending on the degree of serpentinization, the P-wave velocity of the serpentinized peridotite can be in the range from ~5.2 km/s (serpentinite fraction SF: 1.0) to 8 km/s (SF: 0.0) (Miller & Christensen 1997), therefore the observed velocity is well within this range. Multi-channel seismic data from the Atlantic Ocean (Vaddineni et al., 2023) have imaged faulting structure for

642 providing the pathway through which the water can reach the deeper crust. The P-wave velocity
643 in the lower crust comprised of gabbro is usually between 6.6-7.1 km/s (Carlson & Miller 2004;
644 Christeson et al., 2019). The observed velocity sits in the high end. Considering that the gabbroic
645 rocks are mainly composed of Ol, Cpx and plagioclase (Pl) and that the seismic velocities of
646 $V_{Ol} > V_{Cpx} > V_{Pl}$, the observed high velocities could be unaltered primitive gabbro that is rich in
647 Ol or Cpx, which was uplifted from the lower crust. Albeit the presence of abyssal hill
648 morphology on the seafloor may suggest a robust magma supply, the high velocities might
649 indeed be associated with primitive gabbro. In addition, we observe relative large positive and
650 lower negative velocity anomalies near the boundary of abysal hill and St Paul FZ domains,
651 which could be a trace of fault, indicating segment boundary. Large vertical and lateral variations
652 associated with the possible faulting structure can be observed in Figures 9d and 9e close to
653 boundary of zones 1 and 2.

654 **5.3 Zone 3**

655 The segment related to the low basement morphology contains a nearly constant high velocity
656 ranging from 5.5 to 6 km/s commencing near the basement and extending down to a depth of 4
657 km. The dashed green lines in Figure 9e mark the zone boundaries, suggesting the boundary
658 changes with depths. We interpret the lower crust following the 6.5 km/s velocity contour
659 starting from ~ 2 – 3 km depth below the basement. The appearance of 6 km/s near basement and
660 the subtle velocity variations at depth suggest a chemically different composition, compared to
661 the normal oceanic crust. Although we acknowledge that wide-angle OBS data may have limited
662 resolution in the vicinity of the basement due to the lack of turning wave propagation,
663 particularly in areas with rough topography, resolution study implies that the estimated velocities
664 in 3-4 km depth range are reliable (Figures 11 and 12). The nearly constant velocity down to a

665 depth of 4 km suggests it may be hydrated crust containing hydrothermally altered gabbro or can
666 contain altered mantle rocks such as highly serpentinized peridotite. The altered mafic and
667 ultramafic rocks can be emplaced from the greater depths through tectonic activities such as
668 long-lived detachment faulting. Similarly, Davy et al. (2020) observed reduced contrast in the
669 velocity gradient between the upper and lower crust, suggesting a low magma budget and
670 tectonically controlled crustal accretion.

671 **5.4 Zone 4**

672 Zone 4 is located on the northern flank of the Romanche TF, where seafloor dredgings have
673 discovered an extensive occurrence of basaltic and gabbroic rocks. Similar to zone 1, the P-wave
674 velocity show features of a normal oceanic crust with three distinct layers. The velocity of 4.5 –
675 5 km/s near the basement indicates the presence of basaltic rocks. The velocity increases to 6.5 –
676 7 km/s in the lower crust and changes more slowly with depth, suggesting the presence of
677 gabbroic rocks. There are some layered structures in the lower crust (the dashed rectangle in
678 Figure 9d), similar to zone 1, which might be related to layering in the lower crust (Guo et al.,
679 2022).

680

681 Although we have demarcated four distinct zones, the velocity variations from one zone to other
682 is smooth. Therefore, in addition to tectonically controlled segment boundaries, including
683 detachment faults, that could account for the observed strong heterogeneities in the crust, another
684 source to consider is the presence of mantle heterogeneities, i.e., the chemical variations, in the
685 mantle for its parental nature to the oceanic crust. Ubiquitous heterogeneity in the mantle has
686 been well documented by geochemical and geophysical studies (Hart 1988; Lambart et al., 2019;

687 Ritsema & Lekić, 2020), which can play a vital role in melt generation and crustal composition
688 (Shorttle & Maclennan, 2011). Seismic tomography studies suggest the existence of mantle
689 heterogeneities across scales, from 100 km – 1000 km (Ritsema, J., & Lekić, 2020) to on the
690 order of ~10 km (Earle & Shearer 2001). On the Mid-Atlantic Ridge north of the Atlantis TF
691 where mafic and ultramafic plutonic rocks were exposed by detachment faulting, a recent
692 isotopic analysis of Pl and Cpx of drill core gabbroic cumulate (IODP hole U1309D) reveals
693 substantial heterogeneity in the mantle composition (Lambart et al., 2019), much stronger than
694 previous estimation from mid-ocean ridge basalt (MORB) (Hart, 1988). The results also suggest
695 that the mantle melt has limited mixing before being delivered to the crust, supporting in-situ
696 melt crystallization for lower crustal accretion (Boudier et al., 1996; Kelemen et a., 1997; Guo et
697 al., 2022), albeit the composition of MORB suggests that the melt has been homogenized
698 through efficient mixing at the shallow crustal melt lens (Lambart et al., 2019). In north Iceland,
699 also a slow-spreading environment, petrological analysis using basaltic rocks indicates the
700 compositions of enriched and depleted major elements that existed within similar age eruptions
701 from a single volcanic system, indicating a fine-scale mantle source heterogeneity (Shorttle &
702 Maclennan, 2011). Moreover, in the fast-spreading east pacific rise where the oceanic crust is
703 supposedly more homogeneous than the Atlantic, lavas from off-axis seamount contain
704 significant compositional variations ranging from depleted MORB to high enriched MORB at
705 small (~5 km) scales (Anderson et al., 2021), suggesting mantle source heterogeneity. The
706 mantle heterogeneity could be due to small-scale convection along the ridge axis (Ballmer et al.,
707 2011), leading to heterogeneous crustal accretion. For example, in the upwelling region, there
708 would be enhanced magma supply leading to magmatic accretion (e.g. zones 1 and 4) whereas in
709 the downwelling region, there would be reduced magma supply, leading to tectonic accretion

(e.g. zones 2 or 3). Taken together, the heterogeneous oceanic crust in the study region could be formed by an interplay of tectonic, magmatic and hydrothermal processes, enhanced by chemical heterogeneity in the mantle.

6 Conclusions

Applying FWI to the crustal turning waves observed in the OBS data from the equatorial Atlantic Ocean, we have discovered strong heterogeneities in the oceanic crust between the St Paul FZ and the north flank of the Romanch TF. Together with the high-resolution seafloor bathymetry data, we define four distinct zones in the seismic velocity model of the oceanic crust. We observe crustal velocities exhibiting features of a normal oceanic crust associated with the St Paul FZ and the north flank of Romanch TF. The segment underlying the abyssal hills contains a high velocity (~7 km/s) lower crust starting from 2 – 2.5 km depths, possibly containing serpentinised peridotite or unaltered gabbro, and a segment with nearly constant velocity of 5.5-6 km/s from the basement down to 4 km depth, suggesting a hydrated crust. The oceanic crustal heterogeneity along a single segment of ~120 km distance offers a rare window to gain insights for the many factors that play roles for crustal accretion, including magmatic, tectonic and hydrothermal activities, as well as variations in the mantle source composition.

Acknowledgments

The OBS data were acquired during the ILAB-SPARC experiment onboard the French R/V *Pourquoi Pas?* October to November, 2018. This project was funded by the European Research

731 Council Advanced Grant agreement no. 339442 TransAtlanticILAB. This research was funded
732 by the Deep Earth Imaging Future Science Platform, CSIRO. The authors thank Z. Wang and E.
733 Gregory for providing the travel-time picks (used for defining time window of data for FWI). P.
734 Guo thanks Z. Wang for helpful discussion on the raw OBS data.

735

736 **Open Research**

737 The raw OBS data from the OBS12 to OBS15 are available online at the PANGAEA website
738 (https://doi.pangaea.de/10.1594/PANGAEA. 937195) under the condition of acknowledging
739 Growe et al., 2021 (https://doi.org/10.1029/2021JB022456). The OBS data from the OBS16 to
740 OBS20 are available online (https://doi.org/10.1594/PANGAEA. 946565) under the condition of
741 acknowledging Wang et al., 2022 (https://doi.org/10.1038/s41561-022-01003-3). The travel time
742 pickings for the Pg arrivals and the derived velocity models from FWI can be accessed at
743 https://doi.org/10.5281/zenodo.8283195.

744

745

746 **References**

747 Alt, J. C., Laverne, C., Vanko, D. A., Tartarotti, P., Teagle, D. A., Bach, W., ... & Wilkens, R. H.
748 (1996). 34. Hydrothermal alteration of a section of upper oceanic crust in the Eastern Equatorial
749 Pacific: a synthesis of results from site 504 (DSDP LEGS 69, 70, and 83, and ODP LEGS 111,
750 137,140, and 148). In Proceedings of the Ocean Drilling Program, scientific results (Vol. 148,
751 pp. 417-434).

752 Anderson, M., Wanless, V. D., Perfit, M., Conrad, E., Gregg, P., Fornari, D., & Ridley, W. I.
753 (2021). Extreme heterogeneity in mid-ocean ridge mantle revealed in lavas from the 8° 20′ N
754 near-axis seamount chain. Geochemistry, Geophysics, Geosystems, 22(1), e2020GC009322.
755 Arnulf, A. F., Biemiller, J., Lavier, L., Wallace, L. M., Bassett, D., Henrys, S., ... & Plaza
756 Faverola, A. (2021). Physical conditions and frictional properties in the source region of a slow-
757 slip event. Nature Geoscience, 14(5), 334-340.
758 Arnoux, G. M., Toomey, D. R., Hooft, E. E., Wilcock, W. S., Morgan, J., Warner, M., &
759 VanderBeek, B. P. (2017). Seismic evidence that black smoker heat flux is influenced by
760 localized magma replenishment and associated increases in crustal permeability. Geophysical
761 Research Letters, 44(4), 1687-1695.
762 Audhkhasi, P., & Singh, S. C. (2019). Seismic structure of the upper crust from 0–75 Ma in the
763 equatorial Atlantic Ocean on the African plate using ultralong offset seismic data. Geochemistry,
764 Geophysics, Geosystems, 20(12), 6140-6162.
765 Ballmer, M. D., Ito, G., Van Hunen, J., & Tackley, P. J. (2011). Spatial and temporal variability
766 in Hawaiian hotspot volcanism induced by small-scale convection. Nature Geoscience, 4(7),
767 457-460.
768 Bird, P. (2003). An updated digital model of plate boundaries. Geochemistry, Geophysics.
769 Geosystems., 4 (3).
770 Blackman, D. K., & Collins, J. A. (2010). Lower crustal variability and the crust/mantle
771 transition at the Atlantis Massif oceanic core complex. Geophysical Research Letters, 37(24).
772 Bonatti, E. (1968). Ultramafic rocks from the mid-Atlantic ridge. Nature, 219(5152), 363-364.

773 Bonatti, E., Ligi, M., Gasperini, L., Peyve, A., Raznitsin, Y., & Chen, Y. J. (1994). Transform
774 migration and vertical tectonics at the Romanche fracture zone, equatorial Atlantic. Journal of
775 Geophysical Research: Solid Earth, 99 (B11), 21779–21802.
776 Bonatti, E., & Honnorez, J. (1976). Sections of the Earth's crust in the equatorial Atlantic.
777 Journal of Geophysical Research, 81(23), 4104-4116.
778 Boulahanis, B., Carbotte, S. M., Canales, J. P., Han, S., & Nedimović, M. R. (2022). Structure
779 and evolution of northern Juan de Fuca crust and uppermost mantle over the last 8 Ma from an
780 active-source seismic tomography study. Journal of Geophysical Research: Solid Earth, 127(9),
781 e2022JB023987.
782 Boudier, F., Nicolas, A., & Ildefonse, B. (1996). Magma chambers in the Oman ophiolite: fed
783 from the top and the bottom. Earth and Planetary Science Letters, 144(1-2), 239-250.
784 Brocher, T. M. (2005). Empirical relations between elastic wavespeeds and density in the Earth's
785 crust. Bulletin of the seismological Society of America, 95(6), 2081-2092.
786 Canales, J. P. (2010). Small-scale structure of the Kane oceanic core complex, Mid-Atlantic
787 Ridge 23 30′ N, from waveform tomography of multichannel seismic data. Geophysical
788 Research Letters, 37(21).
789 Canales, J. P., Collins, J. A., Escartín, J., & Detrick, R. S. (2000). Seismic structure across the
790 rift valley of the Mid-Atlantic Ridge at 23 20′(MARK area): Implications for crustal accretion
791 processes at slow spreading ridges. Journal of Geophysical Research: Solid Earth, 105(B12),
792 28411-28425.
793 Canales, J. P., Detrick, R. S., Carbotte, S. M., Kent, G. M., Diebold, J. B., Harding, A., ... & Van
794 Ark, E. (2005). Upper crustal structure and axial topography at intermediate spreading ridges:

795 Seismic constraints from the southern Juan de Fuca Ridge. Journal of Geophysical Research:
796 Solid Earth, 110(B12).
797 Cann, J. R., Blackman, D. K., Smith, D. K., McAllister, E., Janssen, B., Mello, S., ... & Escartin,
798 J. (1997). Corrugated slip surfaces formed at ridge–transform intersections on the Mid-Atlantic
799 Ridge. Nature, 385(6614), 329-332.
800 Cannat, M. (1993). Emplacement of mantle rocks in the seafloor at mid-ocean ridges. Journal of
801 Geophysical Research: Solid Earth, 98(B3), 4163-4172.
802 Cannat, M., Lagabrielle, Y., Bougault, H., Casey, J., de Coutures, N., Dmitriev, L., & Fouquet,
803 Y. (1997). Ultramafic and gabbroic exposures at the Mid-Atlantic Ridge: Geological mapping in
804 the 15 N region. Tectonophysics, 279(1-4), 193-213.
805 Carbotte, S. M., Marjanović, M., Carton, H., Mutter, J. C., Canales, J. P., Nedimović, M. R., ... &
806 Perfit, M. R. (2013). Fine-scale segmentation of the crustal magma reservoir beneath the East
807 Pacific Rise. Nature Geoscience, 6(10), 866-870.
808 Carbotte, S. M., Smith, D. K., Cannat, M., & Klein, E. M. (2016). Tectonic and magmatic
809 segmentation of the Global Ocean Ridge System: A synthesis of observations. Geological
810 Society, London, Special Publications, 420(1), 249-295.
811 Carlson, R. L. (2011). The effect of hydrothermal alteration on the seismic structure of the upper
812 oceanic crust: Evidence from Holes 504B and 1256D. Geochemistry, Geophysics, Geosystems,
813 12(9).
814 Carlson, R. L., & Jay Miller, D. (2004). Influence of pressure and mineralogy on seismic
815 velocities in oceanic gabbros: Implications for the composition and state of the lower oceanic
816 crust. Journal of Geophysical Research: Solid Earth, 109(B9).

817 Christeson, G. L., Goff, J. A., & Reece, R. S. (2019). Synthesis of oceanic crustal structure from
818 two-dimensional seismic profiles. Reviews of Geophysics, 57(2), 504-529.
819 Christeson, G. L., McIntosh, K. D., & Karson, J. A. (2007). Inconsistent correlation of seismic
820 layer 2a and lava layer thickness in oceanic crust. Nature, 445(7126), 418-421.
821 Christeson, G. L., Morgan, J. V., & Warner, M. R. (2012). Shallow oceanic crust: Full waveform
822 tomographic images of the seismic layer 2A/2B boundary. Journal of Geophysical Research:
823 Solid Earth, 117(B5).
824 Davy, R. G., Collier, J. S., Henstock, T. J., VoiLA Consortium, Rietbrock, A., Goes, S., ... &
825 Labahn, E. (2020). Wide-angle seismic imaging of two modes of crustal accretion in mature
826 Atlantic Ocean crust. Journal of Geophysical Research: Solid Earth, 125(6), e2019JB019100.
827 Davy, R. G., Frahm, L., Bell, R., Arai, R., Barker, D. H., Henrys, S., ... & Warner, M. (2021).
828 Generating High-Fidelity Reflection Images Directly From Full-Waveform Inversion: Hikurangi
829 Subduction Zone Case Study. Geophysical Research Letters, 48(19), e2021GL094981.
830 Detrick, R. S., Needham, H. D., & Renard, V. (1995). Gravity anomalies and crustal thickness
831 variations along the Mid-Atlantic Ridge between 33° N and 40° N. Journal of Geophysical
832 Research: Solid Earth, 100(B3), 3767-3787.
833 Dick, H. J., Natland, J. H., Alt, J. C., Bach, W., Bideau, D., Gee, J. S., ... & Yoshinobu, A.
834 (2000). A long in situ section of the lower ocean crust: results of ODP Leg 176 drilling at the
835 Southwest Indian Ridge. Earth and planetary science letters, 179(1), 31-51.
836 Dick, H. J., Tivey, M. A., & Tucholke, B. E. (2008). Plutonic foundation of a slow-spreading
837 ridge segment: Oceanic core complex at Kane Megamullion, 23 30′ N, 45 20′ W. Geochemistry,
838 Geophysics, Geosystems, 9(5).

839 Dunn, R. A., Lekić, V., Detrick, R. S., & Toomey, D. R. (2005). Three-dimensional seismic
840 structure of the Mid-Atlantic Ridge (35 N): Evidence for focused melt supply and lower crustal
841 dike injection. Journal of Geophysical Research: Solid Earth, 110(B9).
842 Dunn, R. A., Arai, R., Eason, D. E., Canales, J. P., & Sohn, R. A. (2017). Three-dimensional
843 seismic structure of the Mid-Atlantic Ridge: An investigation of tectonic, magmatic, and
844 hydrothermal processes in the rainbow area. Journal of Geophysical Research: Solid Earth,
845 122(12), 9580-9602.
846 Earle, P. S., & Shearer, P. M. (2001). Distribution of fine-scale mantle heterogeneity from
847 observations of Pdiff coda. Bulletin of the Seismological Society of America, 91(6), 1875-1881.
848 Escartín, J., Mevel, C., Petersen, S., Bonnemains, D., Cannat, M., Andreani, M., ... & Garcia, R.
849 (2017). Tectonic structure, evolution, and the nature of oceanic core complexes and their
850 detachment fault zones (13 20′ N and 13 30′ N, Mid Atlantic Ridge). Geochemistry, Geophysics,
851 Geosystems, 18(4), 1451-1482.
852 Escartín, J., Smith, D. K., Cann, J., Schouten, H., Langmuir, C. H., & Escrig, S. (2008). Central
853 role of detachment faults in accretion of slow-spreading oceanic lithosphere. Nature, 455(7214),
854 790-794.
855 Fichtner, A., Bunge, H. P., & Igel, H. (2006). The adjoint method in seismology: I. Theory.
856 Physics of the Earth and Planetary Interiors, 157(1-2), 86-104.
857 Forbriger, T., Groos, L., & Schäfer, M. (2014). Line-source simulation for shallow-seismic data.
858 Part 1: theoretical background. Geophysical Journal International, 198(3), 1387-1404.
859 Gardner, G. H. F., Gardner, L. W., & Gregory, A. (1974). Formation velocity and density—The
860 diagnostic basics for stratigraphic traps. Geophysics, 39(6), 770-780.

861 Górszczyk, A., Operto, S., & Malinowski, M. (2017). Toward a robust workflow for deep crustal
862 imaging by FWI of OBS data: The eastern Nankai Trough revisited. Journal of Geophysical
863 Research: Solid Earth, 122(6), 4601-4630.
864 Gregory, E. P. M., Singh, S. C., Marjanović, M., &Wang Z. (2021). Evidence for thick mafic
865 crust at the slow-slipping Romanche oceanic transform fault, Geology, G49097.
866 Grevemeyer, I., Ranero, C. R., & Ivandic, M. (2018). Structure of oceanic crust and
867 serpentinization at subduction trenches. Geosphere, 14(2), 395-418.
868 Grevemeyer, I., Hayman, N. W., Peirce, C., Schwardt, M., Van Avendonk, H. J., Dannowski, A.,
869 & Papenberg, C. (2018b). Episodic magmatism and serpentinized mantle exhumation at an
870 ultraslow-spreading centre. Nature Geoscience, 11(6), 444-448.
871 Growe, K., Grevemeyer, I., Singh, S. C., Marjanović, M., Gregory, et al. (2021). Seismic
872 structure of the St. Paul Fracture Zone and Late Cretaceous to Mid Eocene oceanic crust in the
873 equatorial Atlantic Ocean near 18° W. Journal of Geophysical Research: Solid Earth, 126(11),
874 e2021JB022456.
875 Guo, P., Singh, S. C., Vaddineni, V. A., Visser, G., Grevemeyer, I., & Saygin, E. (2021).
876 Nonlinear full waveform inversion of wide-aperture OBS data for Moho structure using a trans-
877 dimensional Bayesian method. Geophysical Journal International, 224(2), 1056-1078.
878 Guo, P., Singh, S. C., Vaddineni, V. A., Grevemeyer, I., & Saygin, E. (2022). Lower oceanic
879 crust formed by in situ melt crystallization revealed by seismic layering. Nature geoscience,
880 15(7), 591-596.
881 Hamilton, E. L. (1978). Sound velocity–density relations in sea-floor sediments and rocks. The
882 journal of the Acoustical Society of America, 63(2), 366-377.

883 Harding, A. J., Kent, G. M., & Orcutt, J. A. (1993). A multichannel seismic investigation of
884 upper crustal structure at 9 N on the East Pacific Rise: Implications for crustal accretion. Journal
885 of Geophysical Research: Solid Earth, 98(B8), 13925-13944.
886 Han, S., Carbotte, S. M., Canales, J. P., Nedimović, M. R., Carton, H., Gibson, J. C., & Horning,
887 G. W. (2016). Seismic reflection imaging of the Juan de Fuca plate from ridge to trench: New
888 constraints on the distribution of faulting and evolution of the crust prior to subduction. Journal
889 of Geophysical Research: Solid Earth, 121(3), 1849-1872.
890 Hart, S. R. (1988). Heterogeneous mantle domains: signatures, genesis and mixing chronologies.
891 Earth and Planetary Science Letters, 90(3), 273-296.
892 Hicks, S. P., Okuwaki, R., Steinberg, A., Rychert, C. A., Harmon, N., Abercrombie, R. E., ... &
893 Sudhaus, H. (2020). Back-propagating supershear rupture in the 2016 M w 7.1 Romanche
894 transform fault earthquake. Nature Geoscience, 13(9), 647-653.
895 Hooft, E. E. E., Detrick, R. S., Toomey, D. R., Collins, J. A., & Lin, J. (2000). Crustal thickness
896 and structure along three contrasting spreading segments of the Mid-Atlantic Ridge, 33.5–35 N.
897 Journal of Geophysical Research: Solid Earth, 105(B4), 8205-8226.
898 Howell, S. M., Olive, J. A., Ito, G., Behn, M. D., Escartin, J., & Kaus, B. (2019). Seafloor
899 expression of oceanic detachment faulting reflects gradients in mid-ocean ridge magma supply.
900 Earth and Planetary Science Letters, 516, 176-189.
901 Iturrino, G. J., Ildefonse, B., & Boitnott, G. (2002). Velocity structure of the lower oceanic crust:
902 Results from Hole 735B, Atlantis II Fracture Zone. In Proc. ODP, Sci. Results (Vol. 176, pp. 1-
903 71). College Station, Tex.: Ocean Drilling Program.
904 Lin, J., & Morgan, J. P. (1992). The spreading rate dependence of three-dimensional mid-ocean
905 ridge gravity structure. Geophysical Research Letters, 19(1), 13-16.

906 Kelemen, P. B., Koga, K., & Shimizu, N. (1997). Geochemistry of gabbro sills in the crust-
907 mantle transition zone of the Oman ophiolite: implications for the origin of the oceanic lower
908 crust. Earth and Planetary Science Letters, 146(3-4), 475-488.
909 Kelemen, P. B., Matter, J. M., Teagle, D. A. H., Coggon, J. A., Oman Drilling Project Science
910 Team, & Oman Drilling Project Science Team. (2020). Site GT3: Sheeted dike to gabbro
911 transition. The Oman drilling Project science team, Proceedings of the Oman drilling Project.
912 Kent, G. M., Harding, A. J., Orcutt, J. A., Detrick, R. S., Mutter, J. C., & Buhl, P. (1994).
913 Uniform accretion of oceanic crust south of the Garrett transform at 14 15′ S on the East Pacific
914 Rise. Journal of Geophysical Research: Solid Earth, 99(B5), 9097-9116.
915 Komatitsch, D., & Martin, R. (2007). An unsplit convolutional perfectly matched layer improved
916 at grazing incidence for the seismic wave equation. Geophysics, 72(5), SM155-SM167.
917 Korenaga, J., Holbrook, W. S., Kent, G. M., Kelemen, P. B., Detrick, R. S., Larsen, H. C., ... &
918 Dahl-Jensen, T. (2000). Crustal structure of the southeast Greenland margin from joint refraction
919 and reflection seismic tomography. Journal of Geophysical Research: Solid Earth, 105(B9),
920 21591-21614.
921 Lambart, S., Koornneef, J. M., Millet, M. A., Davies, G. R., Cook, M., & Lissenberg, C. J.
922 (2019). Highly heterogeneous depleted mantle recorded in the lower oceanic crust. Nature
923 Geoscience, 12(6), 482-486.
924 Luo, Y., & Schuster, G. T. (1991). Wave-equation traveltime inversion. Geophysics, 56(5), 645-
925 653.
926 MacLeod, C. J., Escartin, J., Banerji, D., Banks, G. J., Gleeson, M., Irving, D. H. B., ... & Smith,
927 D. K. (2002). Direct geological evidence for oceanic detachment faulting: The Mid-Atlantic
928 Ridge, 15 45′ N. Geology, 30(10), 879-882.

929 Maia, M., Sichel, S., Briais, A., Brunelli, D., Ligi, M., Ferreira, N., ... & Oliveira, P. (2016).
930 Extreme mantle uplift and exhumation along a transpressive transform fault. Nature Geoscience,
931 9(8), 619-623.
932 Marjanović, M., Singh, S. C., Gregory, E. P., Grevemeyer, I., Growe, K., et al. (2020). Seismic
933 crustal structure and morphotectonic features associated with the Chain Fracture Zone and their
934 role in the evolution of the equatorial Atlantic region. J. Geophys. Res. Solid Earth, 125(10),
935 e2020JB020275.
936 Miller, D. J. & Christensen, N. I. (1997). Seismic velocities of lower crustal and upper mantle
937 rocks from the slow-spreading Mid-Atlantic Ridge, south of the Kane Transform Zone (MARK).
938 Proc. Ocean Drill. Program 153, 437–456.
939 Minshull, T. A., White, R. S., Mutter, J. C., Buhl, P., Detrick, R. S., Williams, C. A., & Morris,
940 E. (1991). Crustal structure at the Blake Spur fracture zone from expanding spread profiles.
941 Journal of Geophysical Research: Solid Earth, 96(B6), 9955-9984.
942 Minshull, T. A., Muller, M. R., Robinson, C. J., White, R. S., & Bickle, M. J. (1998). Is the
943 oceanic Moho a serpentinization front?. Geological Society, London, Special Publications,
944 148(1), 71-80.
945 Morgan, J. P., & Chen, Y. J. (1993). The genesis of oceanic crust: Magma injection,
946 hydrothermal circulation, and crustal flow. Journal of Geophysical Research: Solid Earth,
947 98(B4), 6283-6297.
948 Müller, R. D., Sdrolias, M., Gaina, C., & Roest, W. R. (2008). Age, spreading rates, and
949 spreading asymmetry of the world's ocean crust. Geochemistry, Geophysics, Geosystems, 9(4).
950 Nguyen, B. D., & McMechan, G. A. (2015). Five ways to avoid storing source wavefield
951 snapshots in 2D elastic prestack reverse time migration. Geophysics, 80(1), S1-S18.

952 Nicolas, A., Reuber, I., & Benn, K. (1988). A new magma chamber model based on structural
953 studies in the Oman ophiolite. Tectonophysics, 151(1-4), 87-105.
954 Operto, S., Virieux, J., Dessa, J. X., & Pascal, G. (2006). Crustal seismic imaging from multifold
955 ocean bottom seismometer data by frequency domain full waveform tomography: Application to
956 the eastern Nankai trough. Journal of Geophysical Research: Solid Earth, 111(B9).
957 Pica, A., Diet, J. P., & Tarantola, A. (1990). Nonlinear inversion of seismic reflection data in a
958 laterally invariant medium. Geophysics, 55(3), 284-292.
959 Qin, Y., & Singh, S. C. (2017). Detailed seismic velocity of the incoming subducting sediments
960 in the 2004 great Sumatra earthquake rupture zone from full waveform inversion of long offset
961 seismic data. Geophysical Research Letters, 44(7), 3090-3099.
962 Ritsema, J., & Lekić, V. (2020). Heterogeneity of seismic wave velocity in Earth's mantle.
963 Annual Review of Earth and Planetary Sciences, 48, 377-401.
964 Salisbury, M. H., & Christensen, N. I. (1978). The seismic velocity structure of a traverse
965 through the Bay of Islands ophiolite complex, Newfoundland, an exposure of oceanic crust and
966 upper mantle. Journal of Geophysical Research: Solid Earth, 83(B2), 805-817.
967 Seyler, M., & Bonatti, E. (1997). Regional-scale melt-rock interaction in lherzolitic mantle in the
968 Romanche Fracture Zone (Atlantic Ocean). Earth and Planetary Science Letters, 146(1-2), 273-
969 287.
970 Shipp, R. M., & Singh, S. C. (2002). Two-dimensional full wavefield inversion of wide-aperture
971 marine seismic streamer data. Geophysical Journal International, 151(2), 325-344.
972 Shorttle, O., & Maclennan, J. (2011). Compositional trends of Icelandic basalts: Implications for
973 short–length scale lithological heterogeneity in mantle plumes. Geochemistry, Geophysics,
974 Geosystems, 12(11).

975 Singh, S. C., Collier, J. S., Harding, A. J., Kent, G. M., & Orcutt, J. A. (1999). Seismic evidence
976 for a hydrothermal layer above the solid roof of the axial magma chamber at the southern East
977 Pacific Rise. Geology, 27(3), 219-222.
978 Singh, S. C., Crawford, W. C., Carton, H., Seher, T., Combier, V., Cannat, M., ... & Miguel
979 Miranda, J. (2006). Discovery of a magma chamber and faults beneath a Mid-Atlantic Ridge
980 hydrothermal field. Nature, 442(7106), 1029-1032.
981 Spudich, P., & Orcutt, J. (1980). A new look at the seismic velocity structure of the oceanic
982 crust. Reviews of Geophysics, 18(3), 627-645.
983 Swift, S., Reichow, M., Tikku, A., Tominaga, M., & Gilbert, L. (2008). Velocity structure of
984 upper ocean crust at Ocean Drilling Program Site 1256. Geochemistry, Geophysics, Geosystems,
985 9(10).
986 Tarantola, A. (1984). Inversion of seismic reflection data in the acoustic approximation.
987 Geophysics, 49(8), 1259-1266.
988 Toomey, D. R., Solomon, S. C., & Purdy, G. M. (1994). Tomographic imaging of the shallow
989 crustal structure of the East Pacific Rise at 9° 30′ N. Journal of Geophysical Research: Solid
990 Earth, 99(B12), 24135-24157.
991 Tromp, J., Tape, C., & Liu, Q. (2005). Seismic tomography, adjoint methods, time reversal and
992 banana-doughnut kernels. Geophysical Journal International, 160(1), 195-216.
993 Vaddineni, V. A., Singh, S. C., Grevemeyer, I., Audhkhasi, P., & Papenberg, C. (2021).
994 Evolution of the crustal and upper mantle seismic structure from 0–27 Ma in the equatorial
995 Atlantic Ocean at 2 43′ S. Journal of Geophysical Research: Solid Earth, 126(6),
996 e2020JB021390.

997 Vaddineni, V., Jian, H., & Singh, S. (2023). Seismic evidence for deep hydrothermal circulation
998 and faulting at slow spreading Mid-Atlantic Ridge. Submitted to Nature Geoscience.
999 Vigh, D., & Starr, E. W. (2008). 3D prestack plane-wave, full-waveform inversion. Geophysics,
1000 73(5), VE135-VE144.
1001 Van Avendonk, H. J., Harding, A. J., Orcutt, J. A., & McClain, J. S. (1998). A two-dimensional
1002 tomographic study of the Clipperton transform fault. Journal of Geophysical Research: Solid
1003 Earth, 103(B8), 17885-17899.
1004 Virieux, J. (1986). P-SV wave propagation in heterogeneous media: Velocity-stress finite-
1005 difference method. Geophysics, 51(4), 889-901.
1006 Virieux, J., & Operto, S. (2009). An overview of full-waveform inversion in exploration
1007 geophysics. Geophysics, 74(6), WCC1-WCC26.
1008 Wang, Z., Singh, S. C., Prigent, C., Gregory, E. P., & Marjanović, M. (2022). Deep hydration
1009 and lithospheric thinning at oceanic transform plate boundaries. Nature geoscience, 15(9), 741-
1010 746.
1011 Wang, Z., & Singh, S. C. (2022). Seismic evidence for uniform crustal accretion along slow-
1012 spreading ridges in the equatorial Atlantic Ocean. Nature Communications, 13(1), 7809.
1013 White, R. S., McKenzie, D., & O'Nions, R. K. (1992). Oceanic crustal thickness from seismic
1014 measurements and rare earth element inversions. Journal of Geophysical Research: Solid Earth,
1015 97(B13), 19683-19715.
1016 Wilson, D. S., Teagle, D. A., Alt, J. C., Banerjee, N. R., Umino, S., Miyashita, S., ... & Ziegler,
1017 C. (2006). Drilling to gabbro in intact ocean crust. Science, 312(5776), 1016-1020.

1018 Xu, M., Zhao, X., & Canales, J. P. (2020). Structural variability within the Kane oceanic core
1019 complex from full waveform inversion and reverse time migration of streamer data. Geophysical
1020 Research Letters, 47(7), e2020GL087405.
1021
1022
1023